Nanotechnology, Nonmanufacturing, Nanomaterials

DISC-FETs: Dual Independent Stacked Channel Field-effect Transistors

P. S. Kanhaiya, G. Hills, D. A. Antoniadis, M. M. Shulaker
Sponsors: Analog Devices Inc., NSF, and DARPA

We experimentally demonstrate a three-dimensional (3D) field-effect transistor (FET) architecture leveraging emerging nanomaterials: dual independent stacked channel FET (DISC-FET) (Fig. 1). DISC-FET is composed of two FET channels vertically integrated on separate circuit layers separated by a shared gate. This gate modulates the conductance of both FET channels simultaneously. This 3D FET architecture enables new opportunities for area-efficient 3D circuit layouts. The key to enabling DISC-FET is low-temperature processing to avoid damaging lower-layer circuits.

As a case study, we use carbon nanotube (CNT) FETs (CNFETs) since they can be fabricated at low temperature (e.g., <250 °C). We demonstrate wafer-scale CMOS CNFET-based digital logic circuits: 2-input "not-or" (NOR2) logic gates designed using DISC-FETs with independent NMOS CNT channels below and PMOS CNT channels above a shared gate (Fig. 2 and 3). This work highlights the potential of 3D integration for enabling not only new 3D system architectures, but also new 3D FET architectures and 3D circuit layouts.

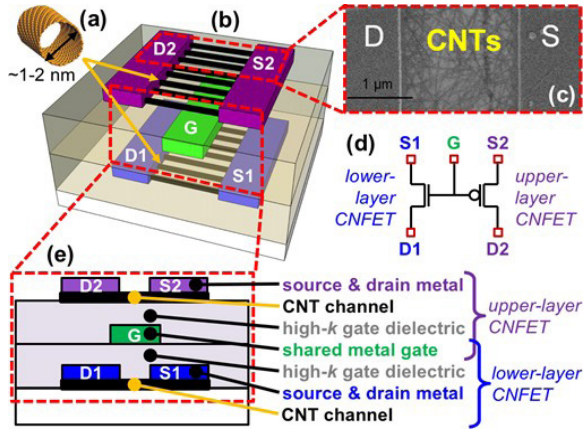

▲Figure 1: CNFET-based DISC-FET. (a) Carbon nanotube (CNT). (b) DISC-FET 3D illustration, including source and drain for the lower-layer CNFET ("S1" and "D1"), source and drain for the upper-layer CNFET ("S2" and "D2"), and shared gate ("G"). (c) Scanning electron microscope (SEM) image of the upper-layer CNFET. (d) 5-terminal circuit schematic of DISC-FET, including 1 PMOS FET and 1 NMOS FET, although each CNFET can be either NMOS or PMOS. (e) Cross-section showing vertically integrated layers.

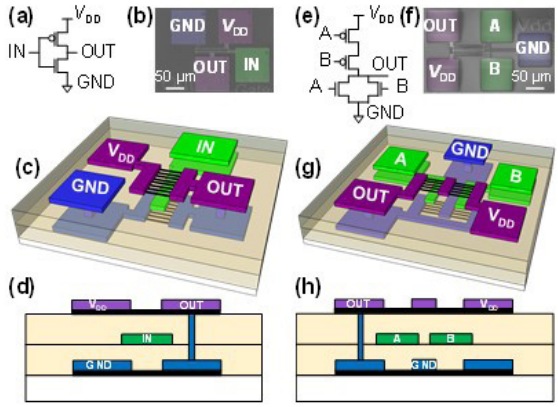

▲Figure 2: Fabricated CNFET-based static CMOS DISC-FET digital logic gates. (a) Inverter schematic, (b) SEM, (c) 3D illustration, and (d) cross-section. (e) 2-input NOR schematic, (f) SEM, (g) 3D illustration, and (h) cross-section.

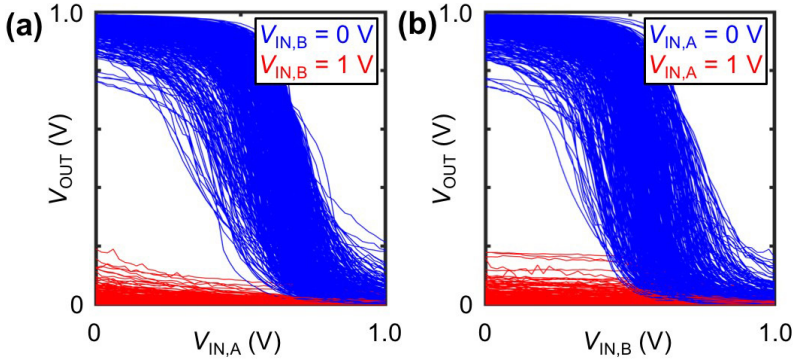

▲Figure 3: Forward sweep VTCs of 500 CNFET-based DISC-FET NOR2 gates (NOR2 design shown in Fig. 3e-f). (a) V_{OUT} vs. V_{IN},A. (b) V_{OUT} vs. V_{IN},B.

Modeling and Optimizing Process Uniformity using Gaussian Process Methods

C. I. Lang, D. S. Boning
Sponsorship: Applied Materials

Modeling process uniformity is critical for achieving the required specifications in many advanced process technologies. For example, sputter deposition systems are prone to significant wafer-scale deposition rate variations due to the complex dynamics of the chamber plasma. Our work focuses on developing and applying machine learning methods for modeling and minimizing these non-uniformities. Traditionally, modeling this process using first physics principles has been particularly difficult due to the chaotic nature of plasma physics. Instead, we model this process using a Gaussian process (GP) framework, which uses historical data to model the deposition rate across the wafer as a function of both process parameters, such as power and chamber pressure, and as a function of the equipment configuration (Figure 1).

Recent work focused on creating a method for optimizing the process parameters and the equipment configuration once a predictive GP model has been fit. As the input space to our process is extremely high-dimensional, many sets of process parameters and equipment configurations may lead to our desired response. For this reason, it is neither possible to explore and model the whole space, nor required to find a configuration that meets our specifications. Therefore, when optimizing a specific process, we search not only for process inputs that lead to our desired response, but also ones that lead to tight confidence intervals (Figure 2), allowing us to accurately model only a portion of the input space and converge on a solution that meets our requirements with relatively few deposition runs. Future work will focus on additional data collection and comparing the convergence rates of our Bayesian optimization method to standard process optimization methods.

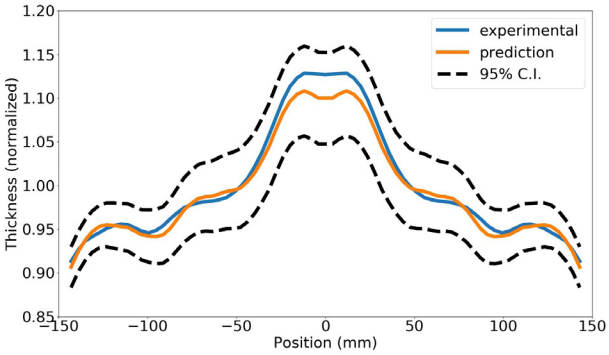

▲ Figure 1: Example of predicted and experimental profiles. The prediction is nearly identical to the experimental thickness, and tight confidence intervals indicate the model's confidence in its prediction.

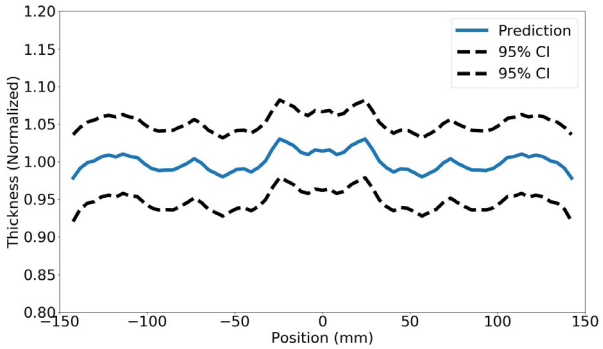

▲ Figure 2: Example of predicted profile after optimization. The optimizer searched for a profile which both reduced thickness non-uniformities and gave tight confidence intervals.

Magic-angle Graphene Superlattices: A New Platform for Strongly Correlated Physics

Y. Cao, D. Rodan-Legrain, O. Rubies-Bigorda, J. M. Park, P. Jarillo-Herrero
Sponsorship: National Science Foundation, Center for Integrated Quantum Materials, Gordon and Betty Moore Foundation, Obra Social "La Caixa"

Understanding strongly correlated quantum matter has challenged physicists for decades. Such difficulties have stimulated new research paradigms, such as ultra-cold atom lattices for simulating quantum materials. Here, we present a new platform to investigate strongly correlated physics, based on graphene moiré superlattices. In particular, when two graphene sheets are twisted by an angle close to the theoretically predicted "magic angle," the resulting flat band structure near the Dirac point gives rise to a strongly correlated electronic system. These flat bands exhibit half-filling insulating phases at zero magnetic field, which we show to be a correlated insulator arising from electrons localized in the moiré superlattice.

Moreover, upon doping this system, we find electrically tunable superconductivity in it, with many characteristics similar to the superconductivity of high-temperature cuprates. These unique properties of magic-angle twisted bilayer graphene open a new playground for exotic many-body quantum phases in a 2D platform made of pure carbon and without a magnetic field. We also present data demonstrating nematicity in the superconducting state, strange metal behavior at correlated fillings with near Planckian dissipation, and correlated states in other types of graphene superlattices. This novel platform may pave the way towards more exotic correlated systems.

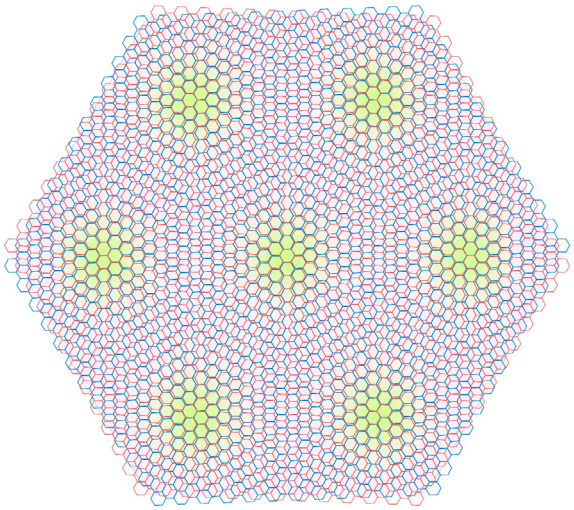

▲Figure 1: Illustration of moiré pattern in twisted bilayer graphene near magic angle and localized density in superlattice (peaking at yellow dots). Displayed twist angle is enlarged for clarity. Larger hexagons, rather than smaller hexagons defined by carbon atoms themselves, become superlattice unit cells.

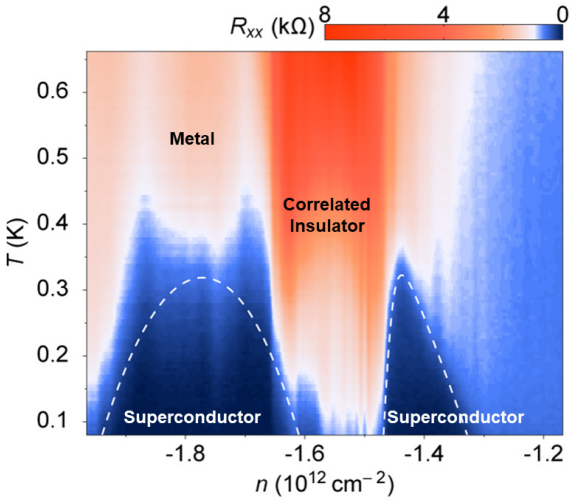

▲Figure 2: Resistance as function of density and temperature. Superconducting domes (blue) appear next to half-filling state, "Correlated Insulator" (red). Magic-angle twisted bilayer graphene offers platform for studying strongly correlated physics and superconductivity with high tunability and accessible critical temperature.

FURTHER READING

- Y. Cao, V. Fatemi, S. Fang, K. Watanabe, T. Taniguchi, E. Kaxiras, and P. Jarillo-Herrero, "Unconventional Superconductivity in Magic-angle Graphene Superlattices," *Nature*, vol. 556, pp. 43–50, Apr. 2018; see also Nature vol. 556, pp. 80–84, Apr. 2018.
- Y. Cao, D. Chowdhury, D. Rodan-Legrain, O. Rubies-Bigorda, K. Watanabe, T. Taniguchi, T. Senthil, and P. Jarillo-Herrero, "Strange Metal in Magic-angle Graphene with near Planckian Dissipation," arXiv:1901.03710, Mar. 2019.
- Y. Cao, D. Rodan-Legrain, O. Rubies-Bigorda, J. Min Park, K. Watanabe, T. Taniguchi, and P. Jarillo-Herrero, "Electric Field Tunable Correlated States and Magnetic Phase Transitions in Twisted Bilayer-Bilayer Graphene," arXiv:1903.08596, Mar. 2019.

Giant Enhancement of Interlayer Exchange in an Ultrathin 2D Magnet

D. R. Klein, D. MacNeill, Q. Song, D. T. Larson, S. Fang, M. Xu, R. A. Ribeiro, P. C. Canfield, E. Kaxiras, R. Comin, P. Jarillo-Herrero

Sponsorship: NSF CIQM, NSF GRFP, Gordon and Betty Moore Foundation, U. S. Department of Energy

A primary question in the emerging field of two-dimensional van der Waals magnetic materials is how exfoliating crystals to the few-layer limit influences their magnetism. Studies on CrI3 have shown a different magnetic ground state for ultrathin exfoliated films, but the origin is not yet understood. Here, we use electron tunneling through few-layer crystals of the layered antiferromagnetic insulator $CrCl_3$ to probe its magnetic order (Figure 1), finding a ten-fold enhancement in the antiferromagnetic interlayer exchange compared to bulk crystals.

Moreover, polarization-dependent Raman spectroscopy (Figure 2) reveals that exfoliated thin films of $CrCl_3$ possess a different low-temperature stacking order than bulk crystals. Temperature-dependent Raman spectra further attribute this difference in stacking to the absence of a stacking phase transition in these thin films, even though it is well established in bulk $CrCl_3$. We hypothesize that this difference in stacking is the origin of the unexpected magnetic ground states in the ultrathin chromium trihalides. Our study provides new insight into the connection between stacking order and interlayer interactions in novel two-dimensional magnets, which may be relevant for correlating stacking faults and mechanical deformations with the magnetic ground states of other more exotic layered magnets, such as $RuCl_3$.

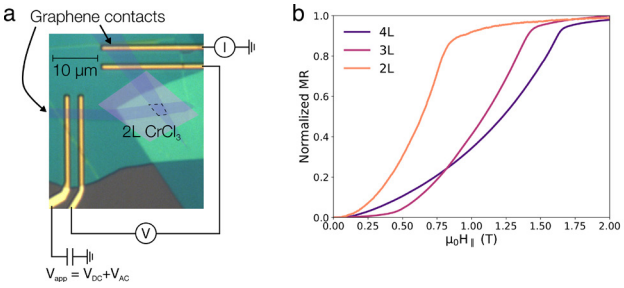

▲Figure 1: (a) False-color optical micrograph of a bilayer $CrCl_3$ tunnel junction device. (b) Normalized magnetoresistance vs. in-plane applied magnetic field for a range of tunnel barrier thicknesses. The plateaus in the magnetoresistance give the saturation fields for different thicknesses of $CrCl_3$.

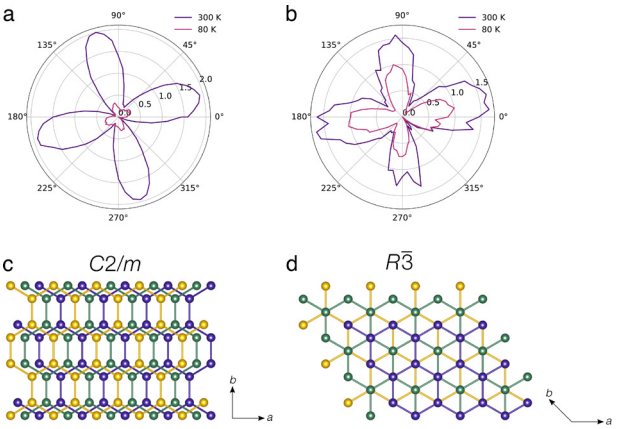

▲Figure 2: Polarized Raman dependence of the 247 cm^{-1} peak energy (in cm-1) for bulk (a) and 17-nm thick (b) $CrCl_3$. Monoclinic stacking (c) corresponds to a fourfold pattern in the Raman data, whereas rhombohedral stacking (d) has no polarization dependence.

FURTHER READING

- B. Huang, G. Clark, E. Navarro-Moratalla, D. R. Klein, R. Cheng, K. L. Seyler, D. Zhong, E. Schmidgall, M. A. McGuire, D. H. Cobden, W. Yao, D. Xiao, P. Jarillo-Herrero, and X. Xu, "Layer-dependent Ferromagnetism in a Van der Waals Crystal Down to the Monolayer Limit," *Nature*, vol. 546, pp. 270-273, 2017.
- D. R. Klein, D. MacNeill, J. L. Lado, D. Soriano, E. Navarro-Moratalla, K. Watanabe, T. Taniguchi, S. Manni, P. Canfield, J. Fernández-Rossier, and P. Jarillo-Herrero, "Probing 2D Magnetism in Van der Waals Crystalline Insulators via Electron Tunneling," *Science*, vol. 360, pp. 1218-1222, 2018.
- D. R. Klein, D. MacNeill, Q. Song, D. T. Larson, S. Fang, M. Xu, R. A. Ribeiro, P. C. Canfield, E. Kaxiras, R. Comin, and P. Jarillo-Herrero, "Giant Enhancement of Interlayer Exchange in an Ultrathin 2D Magnet," [under review], pre-print available at https://arxiv.org/abs/1903.00002, 2019.

Splitting of 2D Materials with Monolayer Precision

J. Shim, S.-H. Bae, W. Kong, D. Lee, J. Kim
Sponsorship: NSF, Office of Naval Research

Traditionally, two-dimensional (2D) heterostructures at the micrometer-scale level are formed by using adhesive tape, which requires isolating 2D flakes in monolayers from bulk material. However, this is a very time-consuming and random process. Moreover, although flakes have been isolated into a nominal monolayer, the lateral dimensions (hundreds of micrometers) are not sufficient to guarantee the fabrication of large-scale 2D heterostructures.

We introduce a layer-resolved splitting (LRS) technique that can be applied universally to harvest multiple 2D material monolayers at the wafer scale (5-centimeter diameter) by splitting single stacks of thick 2D materials grown on a single wafer. Figure 1 shows a schematic of the LRS process. The LRS process is initiated by depositing a Ni film and exfoliating the entire WS_2 stack from the sapphire wafer. A Ni layer is deposited on the bottom of the WS2 film while retaining the top tape/Ni/WS2 stack as-exfoliated to harvest the a continuous WS_2 monolayer. The Ni/WS_2 stack is separated upon peeling while the bottom Ni strongly adheres to the WS_2 monolayer, leaving a monolayer of WS_2 on the bottom Ni layer. We transferred this monolayer film onto an 8-inch (20.3 cm) Si wafer coated with 90 nm of SiO_2 (Figure 2A). Figure 2B shows the wafer-scale photoluminescence mapping image, which indicates that the 2D monolayer isolation was uniform across the entire 2-inch wafer area.

We then fabricated arrays of 2D heterostructure devices at the wafer scale (10x10 arrays of MoS_2 transistors on a 1-cm² wafer) (Figure 2C). The transistors without *h*-BN exhibited very large hysteresis in their drain current-gate voltage sweep, which is detrimental to a transistor's operation. However, substantial suppression of hysteresis has been observed in transistors with *h*-BN (Figure 2D).

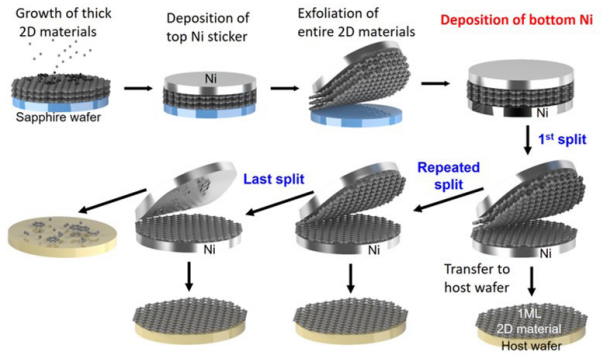

▲Figure 1: Schematic illustration explaining the LRS process.

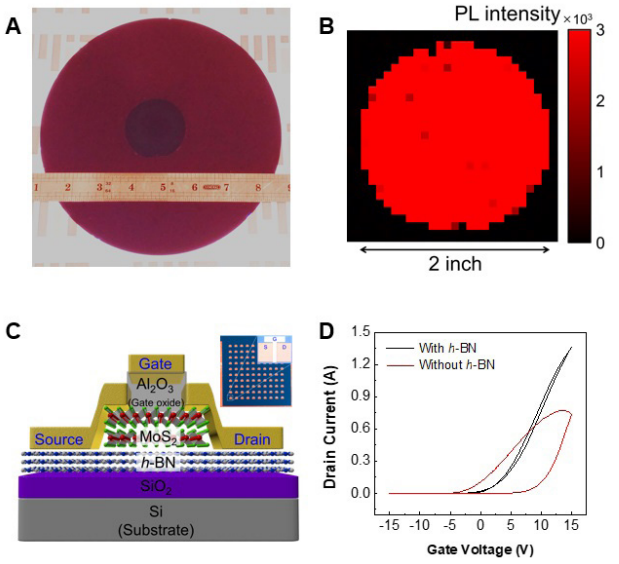

▲Figure 2: A. Optical image of 2-inch wafer-scale WS_2 monolayer on 8-inch SiO_2/Si wafer. B. 2-inch wafer-scale PL mapping image at 1.99 eV of WS_2. C. Schematic illustration of a MoS_2 transistor. D. Representative drain current-gate voltage (I_D–V_G) characteristic curves of MoS_2 transistors with and without *h*-BN inserting layer.

FURTHER READING

- J. Shim, S.-H. Bae, W. Kong, D. Lee, K. Qiao, D. Nezich, Y. Ju Park, R. Zhao, S. Sundaram, X. Li, H. Yeon, C. Choi, H. Kum, R. Yue, G. Zhou, Y. Ou, K. Lee, J. Moodera, X. Zhao, J.-H. Ahn, C. Hinkle, A. Ougazzaden, and J. Kim, "Controlled Crack Propagation for Atomic Precision Handling of Wafer-scale Two-dimensional Materials," *Science*, vol. 362, pp. 665-670, 2018.

Investigation of Atomic Interaction through Graphene via Remote Epitaxy

W. Kong, H. Li, K. Qiao, J. Kim
Sponsorship: Defense Advanced Research Projects Agency, Department of Energy, Air Force Research Laboratory

Remote epitaxy opens the possibility of growing epitaxial films that "copy" the substrate crystal structure through a 2D material interlayer, enabling the production of ultrathin components for device integration. We report advances in understanding the physics of the interaction between the substrate and the epitaxial film.

Remote atomic interaction through 2D materials is governed by the binding nature, that is, the polarity of atomic bonds, both in the underlying substrates and in 2D material interlayers. Although the potential field from covalent-bonded materials is screened by a monolayer of graphene, that from ionic-bonded materials is strong enough to penetrate through a few layers of graphene. The ionicity of the substrate material determines the distance at which its potential field is still effective for epitaxy (Figure 1). However, such field penetration can be substantially attenuated by hexagonal boron nitride (hBN), which itself has polarization in its atomic bonds. A transition from remote epitaxy to van der Waals epitaxy can be seen with an increasing number of hBN layers (Figure 2).

Based on the control of transparency, modulated by the nature of materials as well as interlayer thickness, various types of single-crystalline materials across the periodic table can be epitaxially grown on 2D material-coated substrates. The epitaxial films can subsequently be released as free-standing membranes (Figure 3), which provides unique opportunities for the heterointegration of arbitrary single-crystalline thin films in functional applications.

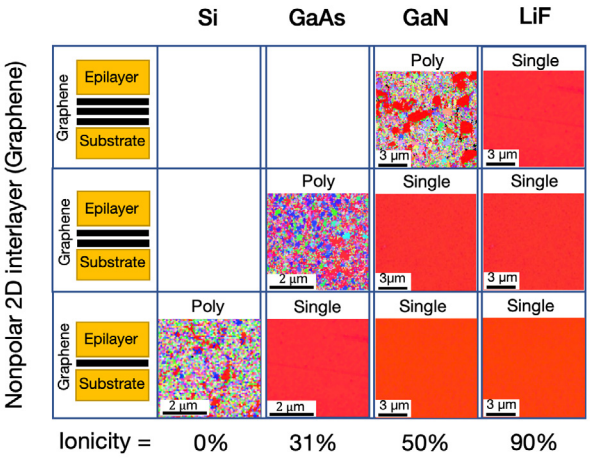

▲ Figure 1: Effect of the polarity of the bulk substrate materials.

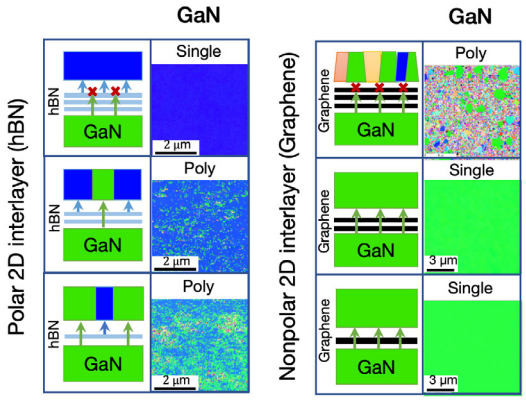

▲ Figure 2: Effect of the polarity of the 2D interlayer materials.

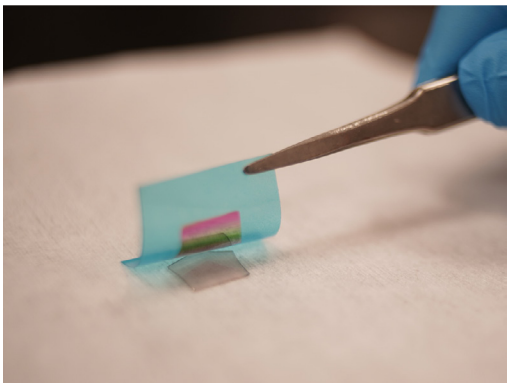

▲ Figure 3: Exfoliation of GaN thin film grown through 2D material.

FURTHER READING

- W. Kong, H. Li, K. Qiao, Y. Kim, K. Lee, Y. Nie, D. Lee, T. Osadchy, R. J Molnar, D. K. Gaskill, R.L. Myers-Ward, K. M. Daniels, Y. Zhang, S. Sundram, Y. Yu, S.-H. Bae, S. Rajan, Y. Shao-Horn, K. Cho, A. Ougazzaden, J. C. Grossman, and J. Kim, "Polarity Governs Atomic Interaction through Two-dimensional Materials," *Nature Materials*, vol. 17, pp. 999-1004, 2018.
- R. Miranda, "Transparency Revealed," *Nature Materials*, vol. 17, pp. 952-953, 2018.

Experimental Characterization and Modeling of Templated Solid-state Dewetting of Thin Single Crystal Films

Y. A. Shin and C. V. Thompson
Sponsorship: National Science Foundation

Templated solid-state dewetting of thin single crystal films has shown potential for use as a self-assembly method for fabrication of regular, complex structures with sub-lithographic length scales (Figure 1 and first Reading below). This potential can be realized by understanding and controlling dewetting instabilities and mechanisms that lead to different dewetting morphologies. Since dewetting instabilities, and hence the resulting morphologies , depend on a number of parameters, including crystal structure of the film (fcc, hcp, etc.), texture of the film, initial film thickness, annealing ambient, temperature, and geometry of the initial template for the film before subject to dewetting, there is a great opportunity/challenge that we are addressing through both experiments and computationally.

During the past several years, we have used prepatterned single-crystal Ni(110) or (100) epitaxial films grown on MgO as a model system and have identified and studied individual dewetting instabilities, including corner-induced instability and Rayleigh-like instability. We are currently focusing on a fingering instability that can occur during edge retraction and results in the formation of a parallel array of wire-like features. An observation motivated our current study that rough edges produced by poor lithographic edge definition led to fingering instabilities. To better understand the effect of edge roughness on the fingering instability and to control the instability, we patterned edges of large Ni(110) lithographically defined patches with a wide range of periodic perturbations. The edges of patches with the same periodic perturbation were also aligned along different crystallographic in-plane orientations to studying anisotropic effects on a templated fingering instability.

We have found that fingering can be induced from those film edges with periodic perturbations (Figure 2), demonstrating that development of the fingering instability has a strong correlation with edge roughness. Furthermore, the template not only induced fingering instabilities but also provided control of the period of the fingers and the corresponding parallel wire-like structures. We have developed a kinetic model that predicts the relationship between the retraction rate of fingers and the templated finger period and are testing this model through additional experiments.

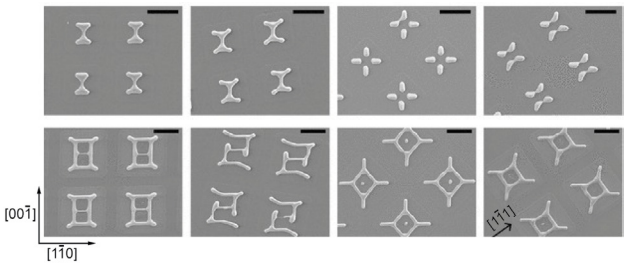

▲ Figure 1: Patterns formed by solid-state dewetting of square patches of Ni films patterned with different sizes and crystallographic orientations, reproduced from first Reading below. Scale: 10 μm.

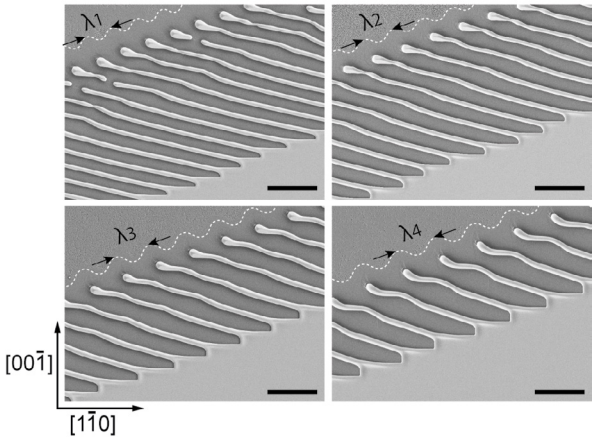

▲ Figure 2: A parallel array of wires with controlled spacing formed by templating a fingering instability using patterned periodic edge roughness in 120-nm-thick Ni(110) films on MgO. λ_1 = 5.36 μm, λ_2 = 6.26 μm, λ_3 = 7.15 μm, λ_4 = 8.05 μm. Scale: 10 μm.

FURTHER READING

- C. V. Thompson, "Solid-state Dewetting of Thin Films," *Annual Review of Materials Research*, vol. 42, pp. 399-434, 2012.
- R. V. Zucker, G. H. Kim, J. Ye, W. C. Carter, and C. V. Thompson, "The Mechanism of Corner Instabilities in Single-crystal Thin Films During Dewetting," *J. Appl. Phys.*, vol. 119, p. 125306, 2016.
- G. H. Kim and C. V. Thompson, "Effect of Surface Energy Anisotropy on Rayleigh-like Solid-state Dewetting and Nanowire Stability," *Acta Materialia*, vol. 84, pp. 190-201, 2015.

Toward Robust, Condensation-resistant, Omniphobic Surfaces

K. L. Wilke, D. J. Preston, Z. Lu, E. N. Wang
Sponsorship: Masdar Institute

Surfaces that are repellent to liquids have broad applications in anti-fouling, chemical shielding, heat transfer enhancement, drag reduction, self-cleaning, water purification, and icephobic surfaces. State-of-the-art omniphobic surfaces based on reentrant surface structures repel all liquids, regardless of the surface material, without requiring low-surface-energy coatings. While omniphobic surfaces have been designed and demonstrated, they fail catastrophically during condensation, a phenomenon ubiquitous in both nature and industrial applications. Specifically, as condensate nucleates within the reentrant geometry, omniphobicity is destroyed.

Here, we show a nanostructured surface that can repel liquids even during condensation (Figure 1). This surface consists of isolated reentrant cavities with a pitch on the order of 100 nanometers to prevent droplets from nucleating and spreading within all structures. We developed a model to guide surface design and subsequently fabricated and tested these surfaces with various liquids. We demonstrated repellency to various liquids up to 10 ˚C below the dew point and showed durability over three weeks. Furthermore, the design is robust to defects or damage to the surface. This work provides important insights for achieving robust, omniphobic surfaces.

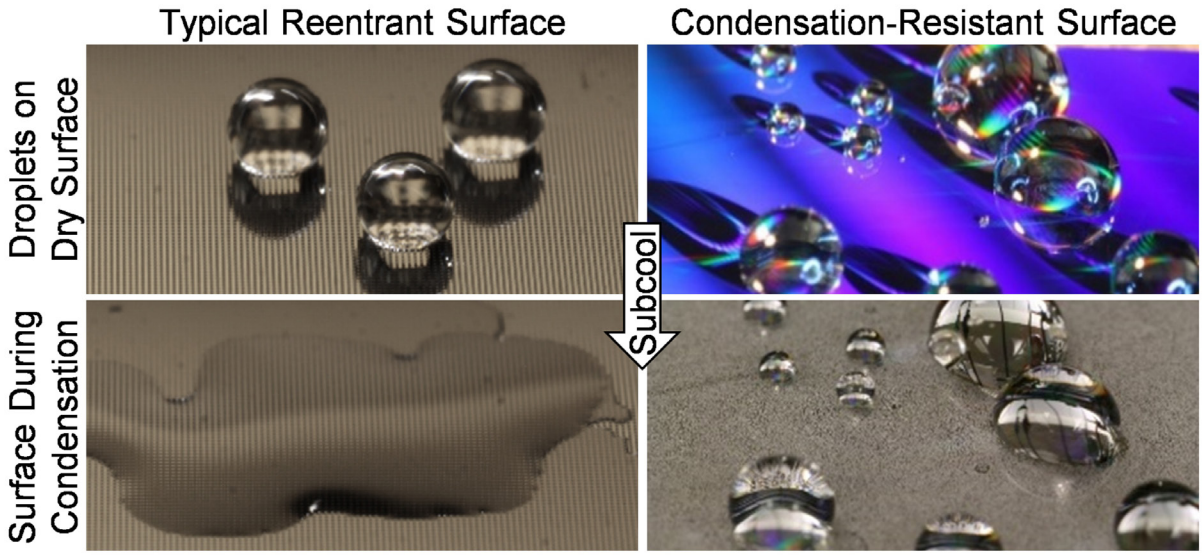

▲ Figure 1: On the left, a typical omniphobic surface repels water when the surface is dry. However, when condensation occurs on the surface, all repellency is lost. On the right, our design using nanometer scale reentrant cavities retains its repellency during condensation.

FURTHER READING

- K. L. Wilke, D. J. Preston, Z. Lu, and E. N. Wang, "Toward Condensation-resistant Omniphobic Surfaces," *ACS Nano*, vol. 12, no. 11, pp. 11013-11021, Oct. 2018.

Observation of Second Sound in Graphite above 100K

S. Huberman, R. Duncan, K. Chen, B. Song, V. Chiloyan, Z. Ding, A. Maznev, G. Chen, K. Nelson
Sponsorship: Office of Naval Research MURI, Department of Energy S3TEC, NSF

Second sound is an unusual phenomenon in which heat transports in a wave-like manner, rather than by the more usual diffusive motion. This wave-like motion is a result of the dominance of normal phonon-phonon scattering, which conserves the total phonon momentum over any other phonon resistive scatterings. Similar to a gas system, where particles scatter without losing total momentum, phonons gain an average velocity under a temperature gradient when normal scattering dominates, and their transport is said to be in the hydrodynamic regime. In this regime, a heat pulse propagates as a wave similar to the way a pressure impulse generates sound waves, and this wave is called second sound. Previously, second sound has been observed in only a few materials at very low temperature (<20 K).

Recently, we successfully predicted and observed second sound in graphite up to 150 K using the transient thermal grating (TTG) technique. In TTG, two transient pump laser beams create interference at the sample surface and generate a thermal grating. A probe beam detects the transient decay of the thermal grating. When the phonon system is diffusive, the thermal grating will decay diffusively with fixed peak and valley positions, corresponding to an exponential decay signal, as shown by the curves at 200 K and 300 K in Figure 1A. However, between 85-150K, the heat wave motion leads to an oscillating exponential signal (hallmark of second sound in TTG), as shown by the curves at 85-150 K. The experimental result is well supported by an ab initio simulation (Figure 1B).

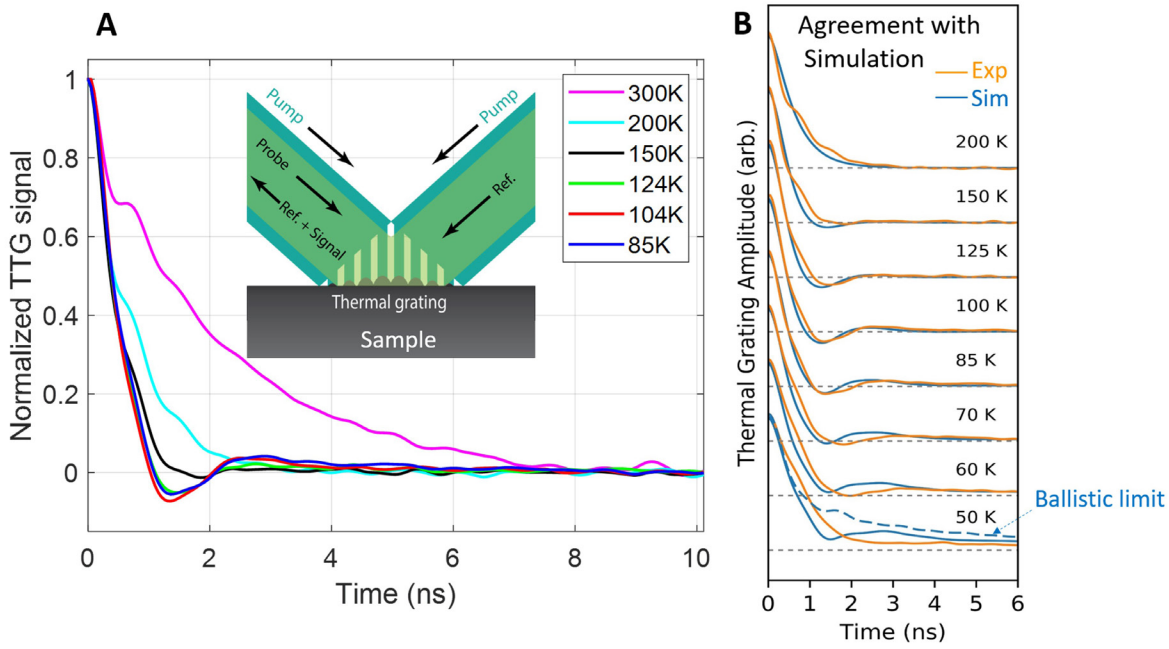

▲ Figure 1: (A) Normalized transient thermal grating signals in graphite at different temperatures. Inset: Schematic illustration of the experiment. (B) Comparison between experimental result and theoretical simulation.

FURTHER READING

- S. Huberman, R. Duncan, et al., "Observation of Second Sound in Graphite at Temperatures above 100 K," *Science*, vol. 364, pp. 375-379, 2019.
- Z. Ding, J. Zhou, et al., "Phonon Hydrodynamic Heat Conduction and Knudsen Minimum in Graphite," *Nano Lett.*, vol. 18, no. 1, pp. 638-649, 2018.
- S. Lee, D. Broido, K. Esfarjani, and G. Chen, "Hydrodynamic Phonon Transport in Suspended Graphene," *Nat. Comm.*, vol. 6, p. 6290, 2015.

Ultrahigh Thermal Conductivity and Mobility in c-BAs

K. Chen, B. Song, A. Schmidt, Z. Ding, T. Liu, G. Chen, in collaboration with Z. Ren (University of Houston), L. Shi (University of Texas – Austin), D. Broido (Boston College)
Sponsorship: Office of Naval Research MURI , Department of Energy S3TEC

As the transistor density gets larger and larger in today's central processing unit, thermal management becomes necessary to improve reliability and prevent overheating failure. Utilizing ultrahigh thermal conductivity materials that can help efficiently dissipate the generated heat from the chips is one of the passive cooling strategies in electronics. In this way, diamond, as the highest thermally conducting material, has been used as the heat spreader. However, diamond is limited by its high cost and interface issues like poor thermal and mechanical coupling to common semiconductors. Therefore, finding other ultrahigh thermal conductivity materials that can totally or partially overcome the limitation of diamond can be significantly beneficial.

Recently, our group with collaborators has predicted, synthesized, and measured ultrahigh thermal conductivity in cubic barium arsenides (c-BAs). First, c-BAs samples of mm-size were successfully synthesized by the chemical vapor transport technique at the University of Houston. With a metal layer coated on top of the sample surface as the transducer, we carried out thermal transport measurements on the samples using time-domain thermoreflectance and frequency-domain thermoreflectance, and the measured thermal conductivity is as high as ~1200 W/mK at room temperature (Figure 1). This places c-BAs as the second most heat-conducting cubic material. In addition, c-BAs is a semiconductor with an indirect bandgap around 1.7 eV. We predict that they have comparably high mobility for both electrons and holes (Figure 2). The high thermal conductivity and high mobility of c-BN promise interesting applications in microelectronics.

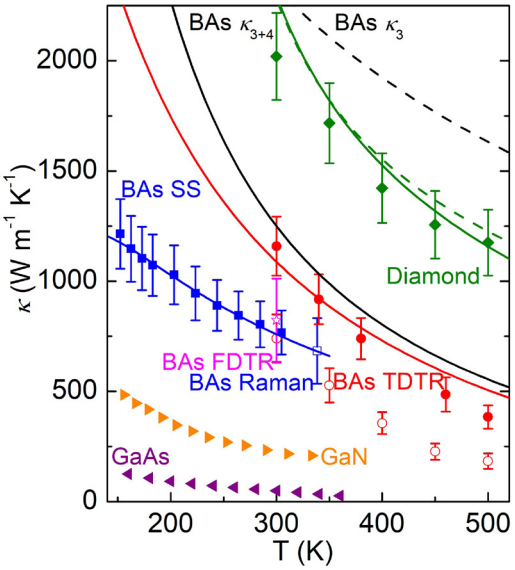

▲ Figure 1: Measured thermal conductivity of BAs in comparison with values from theoretical calculations and other crystals.

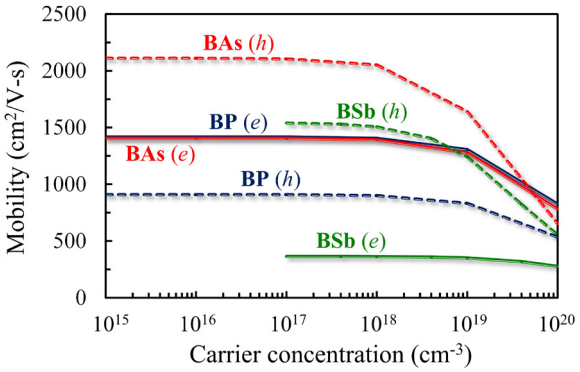

▲ Figure 2: Calculated carrier mobilities of BP (blue), BAs (red), and BSb (green) versus carrier concentrations.

FURTHER READING

- F. Tian, B. Song, X. Chen, et al., "Unusual High Thermal Conductivity in Boron Arsenide Bulk Crystals," *Science*, vol. 361, pp. 582-585, 2018.
- T. Liu, B. Song, L. Meroueh, et al., "Simultaneously High Electron and Hole Mobilities in Cubic Boron-V Compounds: BP, BAs, and BSb," *Phys. Rev. B*, vol. 98, p. 081203(R), 2018.

Morphological Stability of Single Crystal Co and Ru Nanowires

M. A. L'Etoile, Y. A. Shin, W. C. Carter, C. V. Thompson
Sponsorship: National Science Foundation, Semiconductor Research Corporation

High-performance integrated circuits contain tens of kilometers of metal interconnects, the cross-sectional area of which must shrink in lockstep with shrinking transistors. The reliability of integrated circuits is contingent upon morphologically stable interconnects. At the tiny length scales of next-generation interconnects, the electrical resistance of Ru and Co nanowires is expected to be lower than that of nanowires based on current copper technology; thus the morphological stability of these two materials is of particular practical interest. Solid-state dewetting by surface self-diffusion is often the dominant mechanism by which the morphology of micro- and nano-scale features evolve at elevated temperatures. As feature dimensions decrease, the temperature at which dewetting also occurs drops, which can lead to significant morphological degradation at surprisingly low homologous temperatures. Although solid-state dewetting is fairly well understood in isotropic systems, the dewetting behaviors of anisotropic, crystalline solids are far more complicated and more experimental, and modeling work is required to identify crystallographic characteristics that will optimize morphological stability.

Previous work on single-crystal Ni films has demonstrated that crystalline anisotropy gives rise to special crystallographic orientations along which single-crystal wires are kinetically resistant to morphological instabilities. The strongly faceted surfaces of these wires are also predicted to reduce electron scattering and decrease interconnect resistance. For Ru nanowires, exploratory work with single-crystal (0001) films suggests that wires oriented along <1-210> directions will be particularly stable. Work on patterning and testing of such wires is currently underway. We have also begun similar experiments on single-crystal Co films and will compare our results across the Co, Ni, and Ru systems to construct a more fundamental understanding of dewetting behavior in crystalline nano-scale structures such as interconnects.

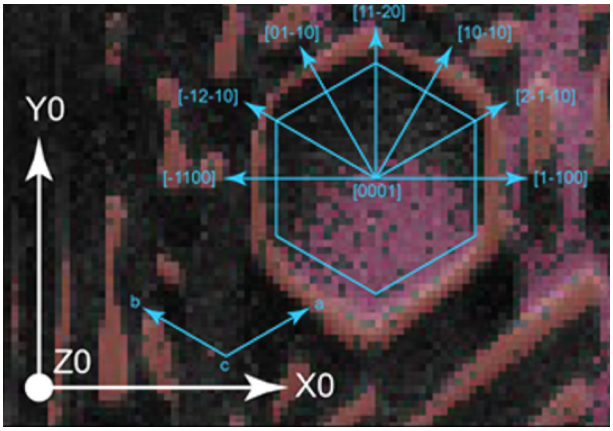

▲Figure 1: Dewetted single-crystal Ru film with features naturally aligned along kinetically stable orientations <1-210>.

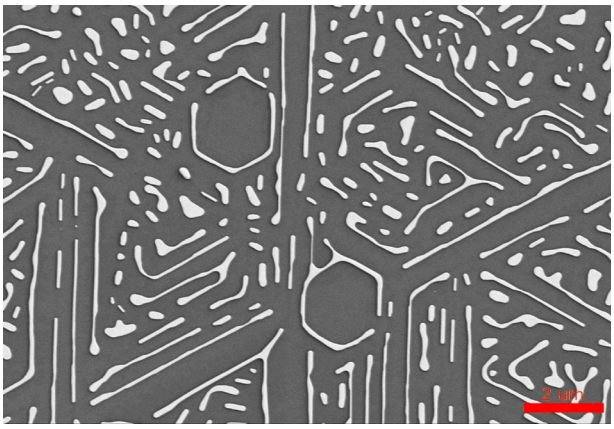

▲Figure 2: Crystallographic map obtained using electron back-scattered diffraction characterization of kinetically stable wire-like features.

FURTHER READING

- G. H. Kim and C. V. Thompson, "Effect of Surface Energy Anisotropy on Rayleigh-like Solid-state Dewetting and Nanowire Stability," *Acta Materiala*, vol. 84, pp. 290-201, Feb. 2015.

Field Controlled Defects in Layered Cuprate-based Materials

C. S. Kim, H. L. Tuller
Sponsor: Skolkovo Foundation

Both the nature and concentration of oxygen defects in oxide materials can have a significant impact on their physical and chemical properties, as well as on key interfacial reaction kinetics such as oxygen exchange with the atmosphere. Most commonly, the desired oxygen defect concentration, or equivalently oxygen nonstoichiometry, is attained by doping with aliovalent cations and/or controlling the oxygen partial pressure and temperature in which the materials are equilibrated or annealed. These approaches, however, are limited by dopant solubility limits and the range of oxygen partial pressures readily experimentally achievable, and they require knowledge of the applicable defect chemical model.

In this study, we fine-tune oxygen defect concentrations in rare earth cuprate (RE_2CuO_4: RE = rare earth) solid oxide fuel cell (SOFC) cathode materials by application of electrical potentials across an yttria-stabilized zirconia (YSZ) supporting electrolyte. These layered perovskites can incorporate both oxygen interstitials, and vacancies, thereby broadening the range of investigations. Here, we show a strong correlation between oxygen nonstoichiometry values (which are determined by in-situ measurement of chemical capacitance) and oxygen surface exchange kinetics (which are inversely proportional to the area-specific-resistance) without changing cation chemistry. Both types of oxygen defects, interstitials and vacancies, dramatically enhance surface kinetics. These studies are expected to provide further insights into the defect and transport mechanisms that support enhanced SOFC cathode performance.

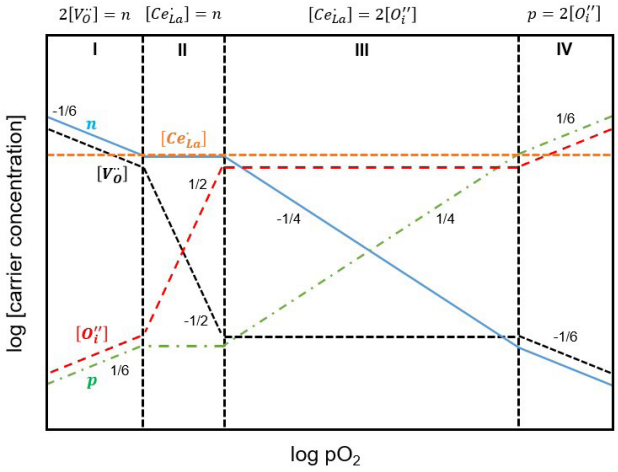

▲ Figure 1: Schematic defect diagram using Brouwer approximation for $La_{1.85}Ce_{0.15}CuO_{4+\delta}$ (LCCO).

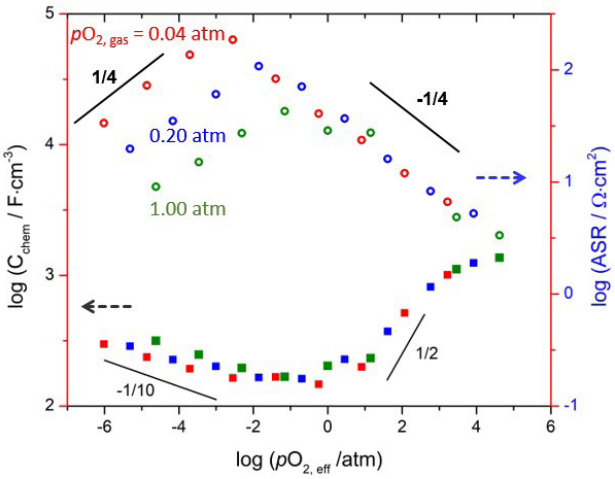

▲ Figure 2: Volumetric chemical capacitance (C_{chem}, closed squares) and area-specific-resistance (ASR, open circles) of an LCCO thin film as functions of effective oxygen partial pressure at 600 °C in log-log plots. Three colors represent three different gas atmospheres ($pO_{2,gas}$ = 1.00 atm, 0.20 atm, and 0.04 atm).

FURTHER READING

- C.-S. Kim and H. L. Tuller, "Fine-tuning of Oxygen Vacancy and Interstitial Concentrations in $La_{1.85}Ce_{0.15}CuO_{4+\delta}$ by Electrical Bias," *Solid State Ionics*, vol. 320, pp. 233-238, Jul. 2018.
- D. Chen and H. L. Tuller, "Voltage-controlled Nonstoichiometry in Oxide Thin Films: $Pr_{0.1}Ce_{0.9}O_{2-\delta}$ Case Study," *Advanced Functional Materials*, vol. 24, no. 48, pp. 7638-7644, Dec. 2014.

Mixed Electron-proton Conductor Membrane Mediates H_2 Oxidation

R. P. Bisbey, B. Yan, W. L. Toh, A. Alabugin, T. S. Wesley, Y. Surendranath
Sponsorship: NSF, MIT Department of Chemistry

Electrochemical transformations are key to the interconversion of electrical and chemical energy and ubiquitous in the formation of commodity chemicals. Electrocatalysts which enable these transformations must serve to both activate chemical bonds and facilitate electron-proton transfer. In conventional electrocatalysis, these two functions occur at a singular catalyst electrolyte interface that prevents independent optimization of either process; changes to the interface will inherently affect both functions. Critically, the optimal interface for one function often does not coincide with the optimal structure for the other. We have shown that for hydrogen oxidation reaction (HOR), these two functions can be segregated by interposing a mixed electron-proton conductor (MEPC) membrane between the catalyst and electrolyte.

We have designed a device that enables concurrent electrochemical proton-electron extraction at an MEPC electrolyte interface and H2 activation at a gas catalyst interface. A reduced WO_3 (WO_x) membrane supported on a porous support is decorated with a platinum catalyst on one side (Figure 1). At the gas Pt interface, H_2 is dissociatively activated at Pt surfaces to generate H-atoms. The resulting H-atoms migrate across the Pt WO_x boundary to intercalate into the WO_x via H-spillover and diffuse through the WO_x membrane. At the MEPC electrolyte interface, the applied electrochemical potential drives the separation of protons and electrons with protons entering the solution and electrons passing current through the external circuit. This work represents the first demonstration of employing an MEPC membrane to segregate the bond activation and charge transfer functions in electrocatalysis.

These devices exhibit respectable current densities that exceed 20 mA cm^{-2} at 0.5 V vs. RHE. We found that the thickness of the membrane does not limit the rate of H2 oxidation catalysis, suggesting that H-diffusion within the WO_x membrane is relatively rapid. Instead, the condensed MEPC membrane serves as a barrier to prevent impurities and poisoning species dissolved in the electrolyte to degrade HOR catalysis. On the other hand, the rate of HOR depends on the Pt sputtering time (Figure 2). An increasing rate was found, up to 35 s of Pt deposition, which decreased upon continued sputtering. This suggests that H-spillover across the Pt WO_x boundary limits the overall rate of HOR and a 35 s deposition of Pt maximizes the Pt WO_x boundary line density. Future work focuses on a selection of materials for these devices to enable a library of diverse reactivity.

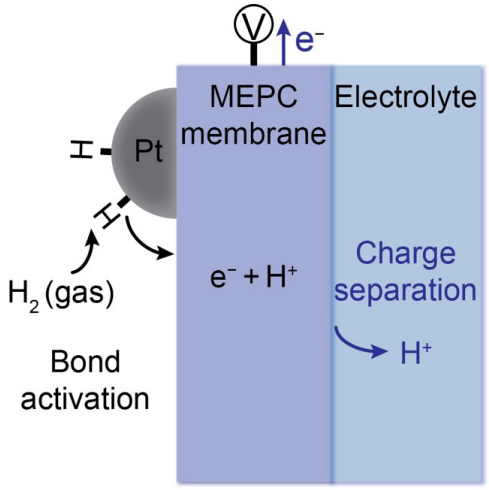

▲ Figure 1: Schematic of hydrogen oxidation reaction enabled by Pt MEPC composite electrode. H_2 is supplied to the Pt catalyst and is ultimately oxidized at the polarized electrolyte interface.

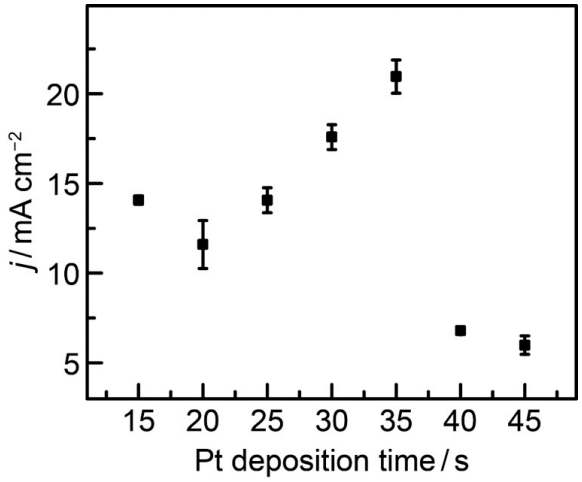

▲ Figure 2: Dependence of the current density of devices at 0.5 V (vs. RHE) on Pt sputtering time, indicating that H-spillover occurring at the Pt WO_3 phase boundary limits the reaction rate.

FURTHER READING

- B. Yan, R. P. Bisbey, A. Alabugin, and Y. Surendranath, "Mixed Electron-Proton Conductors Enable Spatial Separation of Bond Activation and Charge Transfer in Electrocatalysis," *J. Amer. Chem. Soc.*, 2019.
- R. Prins, "Hydrogen Spillover. Facts and Fiction," *Chem.* Rev., vol. 112, p. 2714, 2012.
- P. M. S. Monk, "Charge Movement through Electrochromic Thin-film Tungsten Trioxide," *Crit. Rev. Solid State Mater. Sci.*, vol. 24, p. 193, 1999.

Dynamic Approach of Quantifying Strain Effects on Ionic and Electronic Defects in Functional Oxides

Y.-T. Chi, T. Defferriere, H. L. Tuller, B. Yildiz, and K. Van Vliet
Sponsorship: U.S. Department of Energy, Basic Energy Sciences

The search for novel electronic and magnetic properties in functional oxides has generated a growing interest in understanding the mobility and stability of ionic and electronic defects in these materials. Instead of altering material content, most research views mechanical strain as a lever for modulating defect concentration and mobility more finely and continuously in both semiconductors and function-al oxides. Previous studies also proposed that strain may increase ionic mobility by orders of magni-tude, which is crucial for lowering the operation temperature of solid oxide fuel cells.

However, experimental and computational results differ significantly among research groups due to the convoluted effect of mechanical strain and film/substrate interface on defect content and mobility. Such reliance on substrate selection to induce strain in the oxide thin film also limits the range of strain accessible, with limited data available to date.

We have developed an experimental technique that facilitates application of in-plane strain to functional oxide thin films continuously on the same substrate. First, we combine photolithography and metal sputtering to deposit an interdigitated Pt electrode on our sample (Figure 1). Next, we conduct 3- or 4-point bending and concurrent conductivity measurement of the thin film-on-substrate device (Figure 2). This approach is accessible to a wide temperature range and precise gas control relevant to mixed ionic-electronic conducting oxides. We can strain and measure the transport properties of the same functional oxide thin film at high temperature in situ, over a range of strains applied to a single system. Combining these experiments with our ab initio computational simulations and predic-tions of carrier dominance over a range of strains and temperatures, we also aim to measure the carri-er mobility in Nb-doped SrTiO3 as a function of applied strain, to observe the sudden change of carrier mobility and temperature dependency. We believe this will also be a powerful technique for studying the strain effect on surface reactions like exsolution or catalytic reaction.

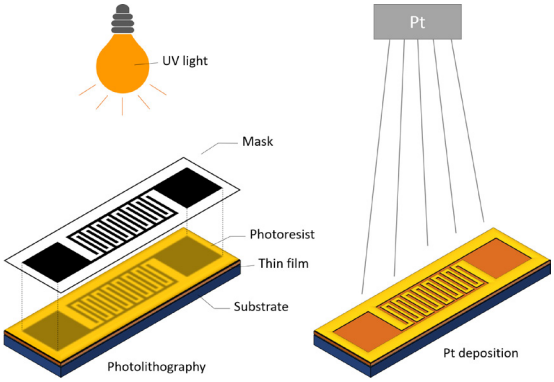

▲Figure 1: Photolithography for interdigitated electrode pattern on photoresist, followed by Pt deposition using sputtering.

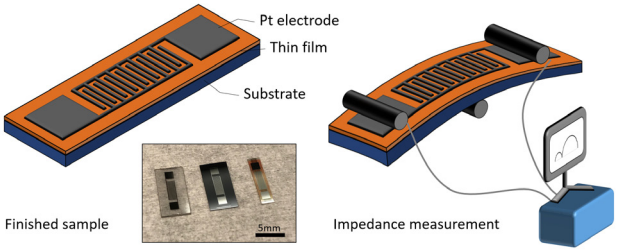

▲Figure 2: Finished sample with interdigitated Pt electrode. Yttria-doped zirconia, Nb-doped $SrTiO_3$ and Pr-doped CeO_2 (left to right). Impedance measurement with 3-point bending on the sample.

FURTHER READING

- Y.-T. Chi, M. Youssef, L. Sun, K. J. Van Vliet, and B. Yildiz, "Accessible Switching of Electronic Defect Type in SrTiO3 via Biaxial Strain," *Physical Review Materials*, vol. 2 , issue no. 5, pp. 055801:1-8, 2018.

3-D Printed Microarchitected Ceramics for Low-heat Capacity Reactors

S. Kim, T. Ganapathy, W. Kim, Y. T. Cho, N. X. Fang
Sponsorship: MIT Energy Initiative

Efficient heat and mass transfer for catalytic reactors are desirable for a broad array of biological and environmental applications and are of great import to the automotive and power plant industry. The conversion efficiency of catalytic reactors relies on the temperature of the constituent substrate and its thermal response.

Although porous substrates with thinner cell/pore walls and higher cell/pore density enable faster catalyst activation due to low thermal mass and, larger surface area, the manufacturing of well-engineered structures with thin walls and higher cell/pore density remains a challenge. For example, there is a practical limit to the maximum cell density and the minimum wall thickness of the honeycomb substrate caused by difficulties in the extrusion-based process, such as larger flow drag force and inhomogeneity. Another promising candidate, the open-cell foams, also suffer manufacturing and assembly difficulties due to their low mechanical strength, high flow resistance, and high heat capacity caused by random-pore architectures.

To overcome these limitations, we proposed manufacturing-friendly structural design and additive manufacturing for microarchitected ceramic substrates having both a large catalytic surface area and low thermal mass. Our idea for achieving efficient catalytic substrates is leveraging 3D micro-lattices of thin-walled tubular networks instead of conventional honeycomb monoliths (Figure 1). We measured surface temperature by thermal IR camera (Figure 1) and investigated the thermal response of each architecture (Figure 2). The proposed 3D hollow micro-lattice was heated up and cooled down faster than the monoliths' structure. This result verifies the low thermal mass of the proposed 3D micro-lattice ceramic to enable a faster thermal response for the faster catalytic activation. Therefore, we expect that the proposed 3D ceramic micro-lattice structure will have a high catalytic conversion efficiency and accelerate the development of an efficient gas purification system for automotive and environmental applications.

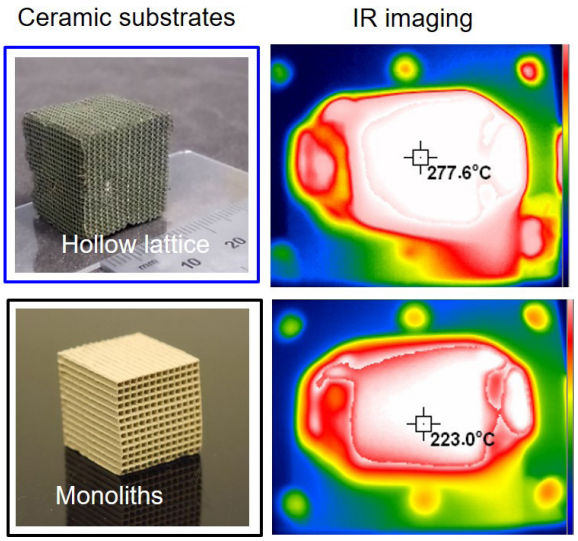

▲Figure 1: Optical microscope and thermal infrared (IR) camera images of 3D hollow micro-lattice ceramic and commercial honeycomb monoliths ceramic.

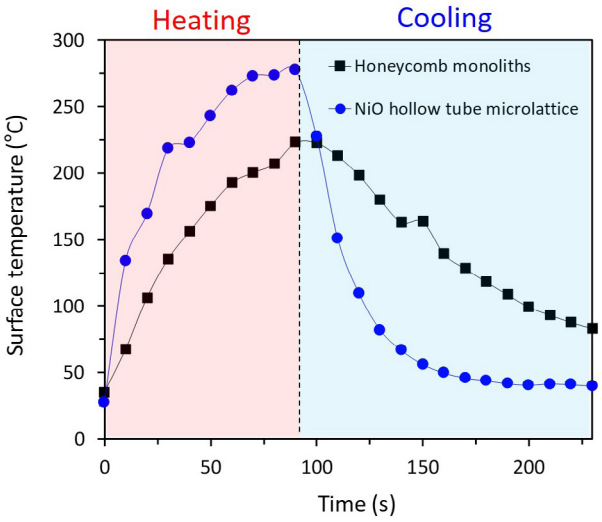

▲Figure 2: Surface temperature was experimentally measured by IR imaging at air-flow heating (flow rate, 21.24 L/min) with temperature of 650 °C and cooling in atmosphere.

FURTHER READING

- X. Zheng, H. Lee, T. H. Weisgraber, M. Shusteff, J. DeOtte, E. B. Duoss, J. D. Kuntz, M. M. Biener, Q. Ge, J. A. Jackson, S. O. Kucheyev, N. X. Fang, and C. M. Spadaccini, "Ultralight, Ultrastiff Mechanical Metamaterials," *Science*, vol. 344, pp. 1373-1377, 20, Jun. 2014.
- C. S. Roper, R. C. Schubert, K. J. Maloney, D. Page, C. J. Ro, S. S. Yang, and A. J. Jacobsen, "Scalable 3D Bicontinuous Fluid Networks: Polymer Heat Exchangers toward Artificial Organs," *Adv Mater.*, vol. 27, pp. 2479-2484, 17, Apr. 2015.
- C. Parra-Cabrera, C. Achille, S. Kuhn, and R. Ameloot, "3D Printing in Chemical Engineering and Catalytic Technology: Structured Catalysts, Mixers, and Reactors," *Chem. Soc. Rev.*, vol. 47, pp. 209-230, 2018.

Additively Manufactured Externally-fed Electrospray Sources

D. V. Melo-Máximo, S. Lin, and L. F. Velásquez-García
Sponsorship: MIT-Tecnologico de Monterrey Nanotechnology Program

Additive manufacturing (AM) is a layer-by-layer fabrication technique that creates solid objects by putting material where needed, instead of removing material from stock. Recent advances in AM have made possible the implementation of microsystems that surpass the performance of state-of-the-art counterparts made in a clean room, as well as the demonstration of devices that are challenging or unfeasible to create using standard microfabrication–particularly in the area of microfluidics. In addition, AM is inherently compatible with implementing, with great precision, hierarchical structures with features spanning orders of magnitude in size to accomplish multiple tasks efficiently.

In this project, we are exploring AM to develop, at a low-cost, massively multiplexed externally-fed electrohydrodynamic liquid ionizers (Figure 1) for a wide range of applications such as mass spectrometry, nanosatellite propulsion, species transport, and agile manufacturing. These devices are mesoscaled arrays of high-aspect-ratio, hundreds-of-microns tall, micron-sharp tips that are conformally covered with a nanostructured layer that transports and regulates the flow of liquid from the reservoir to the emission sites. Manufacturing issues such as interprocess compatibility and tip array uniformity need to be addressed to implement devices that operate efficiently successfully. Current work focuses on exploring and optimizing various manufacturing techniques to monolithically create the electrospray source out of different structures made of different materials; future work includes assessment of device performance, e.g., emission characteristics and uniformity.

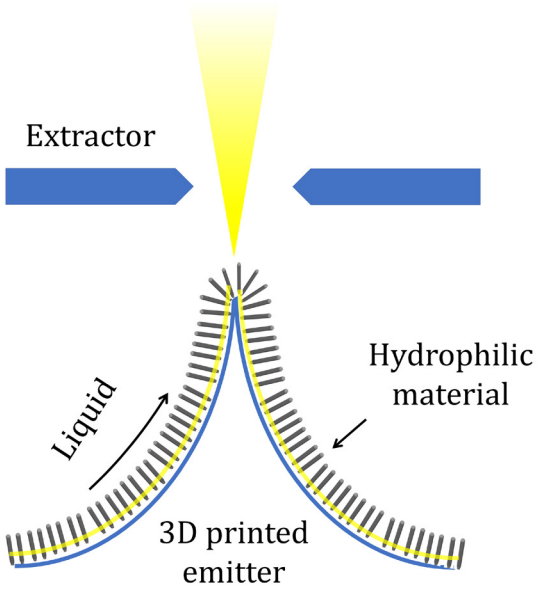

▲ Figure 1: Schematic of an externally-fed emitter

FURTHER READING

- D. I. Wimpenny, P. M. Pandey, and L. J. Kumar, "Advances in 3D Printing & Additive Manufacturing Technologies," *Springer*, 2017.
- B. Gassend, L. F. Velásquez-García, A. Ibitayo Akinwande, and M. Martínez-Sánchez, "A Microfabricated Planar Electrospray Array Ionic Liquid Ion Source with Integrated Extractor," *J. of Microelectromechanical Systems*, vol 18, Issue: 3, pp. 679–694, 2009.
- F. A. Hill, E. V. Heubel, P. J. Ponce de Leon, and L. F. Velásquez-García, "High-throughput Ionic Liquid Ion Sources using Arrays of Microfabricated Electrospray Emitters with Integrated Extractor Grid and Carbon Nanotube Flow Control Structures," *J. of Microelectromechanical Systems*, vol. 23, no. 5, pp. 1237–1248, Oct. 2014.

Additive Manufacturing of Microfluidics via Extrusion of Metal Clay

E. Segura-Cardenas, L. F. Velásquez-García
Sponsorship: MIT-Tecnologico de Monterrey Nanotechnology Program

Most microfluidics uses closed microchannels to efficiently accomplish tasks such as species mixing, heat transfer, and particle sorting by increasing the surface-to-volume ratio of the fluid(s) involved in the process. However, the current manufacturing techniques for microfluidics present disadvantages such as high-cost, long production time, no device customization, elaborated design iteration, restriction in the kinds of structures that can be made, and low fabrication yield.

Recent research results demonstrate that additive manufacturing can readily address the shortcomings outlined, often yielding devices that surpass the state of the art or for which traditional microfabrication creates no counterpart. However, most 3D-printed microfluidics are made of polymeric feedstock, which is not compatible with high-pressure and/or high-temperature applications. Mainstream 3D printing methods for metal include lost-wax micro molding, inkjet binder, and direct metal laser sintering; these processes are unideal to produce monolithic closed-channel microfluidics because they either require internal dummy structures or create internal voids filled in with unprocessed printable material, both of which are challenging to remove from the printed part.

In this project, we are exploring the use of extrusion of metal clay to implement closed-channel microfluidics; the technique is arguably similar to fused filament fabrication and can readily create voids without spurious infill or post-processing required. Via the extrusion of metal clay, leak-tight metal microchannel with monolithic, working ports have been created (Figure 1). A cross-section of the microfluidic shows an unclogged microchannel, evidencing the feasibility of the technique to create closed channels with hydraulic diameters of relevance to microfluidics (Figure 2). Current work focuses on exploring the design space of the technology and demonstrating an application of relevance.

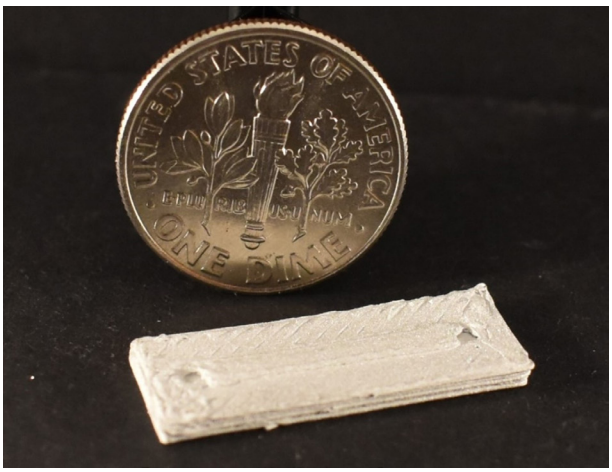

▲ Figure 1: Extruded monolithic microfluidic with 350-µm wide and 350-µm tall microchannel and inlet and outlet ports.

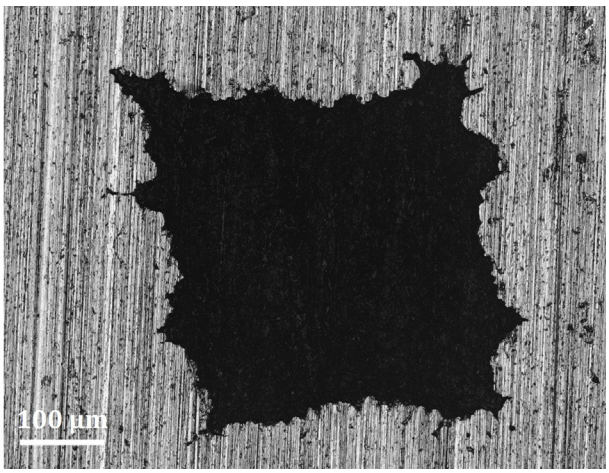

▲ Figure 2: Cross section of closed microchannel.

FURTHER READING

- R. Frykholm, Y. Takeda, B. G. Andersson, and R. Carlström, "Solid State Sintered 3-D Printing Component by using Inkjet (Binder) Method," *J. of the Japan Society of Powder and Powder Metallurgy*, vol. 63, no. 7, pp. 421–426, 2016.
- Z. Sun, G. Vladimirov, E. Nikolaev, and L. F. Velásquez-García, "Exploration of Metal 3-D Printing for the Microfabrication of Freeform, Finely Featured, Mesoscaled Structures," *J. of Microelectromechanical Systems*, vol. 27, no. 6, pp. 1171 - 1185, Dec. 2018.
- S. Marre, J. Baek, J. Park, M. G. Bawendi, and K. F. Jensen, "High-Pressure/High-Temperature Microreactors for Nanostructure Synthesis," *JALA: J. of the Association for Laboratory Automation*, vol. 14, no. 6, pp. 367–373, Dec. 2009.

3D-Printed, Low-cost, Miniature Liquid Pump

A. P. Taylor, L. F. Velásquez-García
Sponsorship: Edwards Vacuum

Many compact systems use pumps to precisely set flow rates of liquid or, in general, to manipulate small liquid volumes for effective mass transport, cooling, or momentum transfer. Numerous microfabricated positive displacement pumps for liquids with chamber volumes that are cycled using valves have been proposed. Pumps made via standard (i.e., cleanroom) microfabrication typically cannot deliver large flow rates without integrating hydraulic amplification or operating at high frequency due to their small pump chambers.

Additive manufacturing, i.e., the layer-by-layer fabrication of objects using as template a computer-aided design model, has recently been explored as a processing arena for microsystems. In particular, researchers have reported 3-D printed pumps for liquids and gases with performance on par or better than counterparts made with standard microfabrication. Building upon earlier work on printed MEMS magnetic actuators, we recently developed miniature liquid pumps printed in pure nylon 12 via fused filament fabrication (FFF) whereby a thermoplastic filament is extruded from a hot nozzle to create a solid object layer by layer.

Our low-cost, leak-tight, miniature devices are microfabricated using 150- to 300-µm layers with a multi-step printing process (Figure 1) that monolithically creates all key features with <13- µm in-plane misalignment. Each pump has a rigid frame, a 21-mm-diameter, 150-µm-thick membrane connected at its center to a piston with an embedded magnet, chamber, passive ball valves, and two barbed fluidic connectors (Figure 2). Pump fabrication under 2 hours and costs less than $4.65 are achieved. Finite element analysis of the actuator predicts a maximum stress of 18.7 MPa @ 2-mm deflection, about the fatigue limit of nylon 12 (i.e., 19 MPa). A maximum water flow rate of 1.37 ml/min at 15.1 Hz actuation frequency is calculated, comparable to reported values of miniature liquid pumps with up to 200X higher actuation frequency.

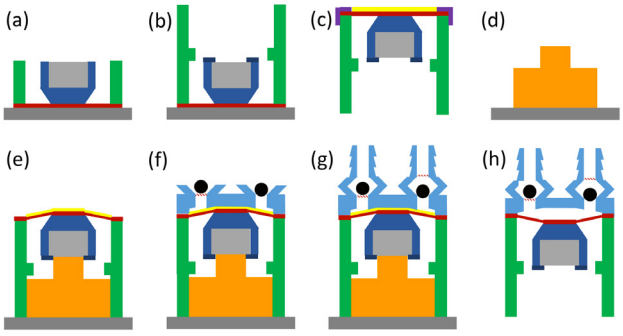

▲Figure 1: Half is printed (a)-(b) with membrane (red) and inserted magnet (grey). Partial pump is prepared, (c)-(e); second half printed on top, (f)-(h) with chamber (light blue), valve grids (red hatch), inserted balls (black).

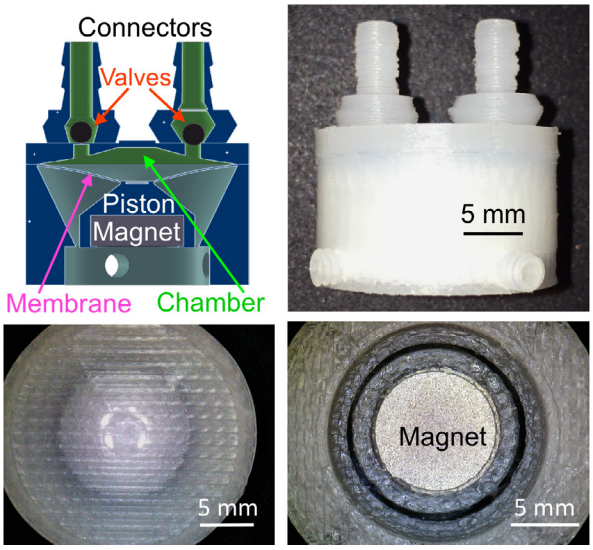

▲Figure 2: Clockwise from upper left: cross section of pump model; side view of printed pump; bottom view of printed pump with embedded SmCo magnet; top view of pump membrane, prior to printing second half.

FURTHER READING

- A. P. Taylor and L. F. Velásquez-García, "Miniaturized Diaphragm Vacuum Pump by Multi-material Additive Manufacturing," *J. Microelectromech. Syst.*, vol. 26, no. 16, pp. 1316-1327, Dec. 2017.
- A. P. Taylor and L. F. Velásquez-García, "High-temperature Compatible, Monolithic, 3D-Printed Magnetic Actuators," *J. Phys. Conf. Ser.*, vol. 1052, 012046 (4 pp), Jul. 2018.
- A. P. Taylor and L. F. Velásquez-García, "Low-cost, Monolithically 3D-Printed, Miniature High-flow Rate Liquid Pump," *PowerMEMS 2018 Conference Proceedings*, Dec. 2018.

3D-Printed Microfluidics to Evaluate Immunotherapy Efficacy

A. L. Beckwith, J. T. Borenstein, L. F. Velásquez-García
Sponsorship: Draper

Microfluidic devices are conceptually an ideal platform for the provision of personalized medical evaluations as they require small analyte volumes and facilitate rapid and sensitive investigations. However, inherent challenges in device fabrication have impeded the widespread adoption of microfluidic technologies in the clinical setting. Additive manufacturing could address the constraints associated with traditional microfabrication, enabling greater microfluidic design complexity, fabrication simplification (e.g., removal of alignment and bonding process steps), manufacturing scalability, and rapid and inexpensive design iterations.

We have developed an entirely 3D-printed microfluidic platform that enables modeling of interactions between tumors and immune cells, providing a microenvironment for testing the efficacy of immunotherapy treatment. The monolithic platform allows for real-time analysis of interactions between a resected tumor fragment and resident or circulating lymphocytes in the presence of immunotherapy agents. Our high-resolution, non-cytotoxic, transparent device monolithically integrates a variety of microfluidic components into a single chip, greatly simplifying device operation vs. traditionally-fabricated microfluidic systems. The 3D-printed device sustains viability of biopsied tissue fragments under dynamic perfusion for at least 72 hours while enabling simultaneous administration of drug treatments, illustrating a useful tool for drug development and precision medicine for immunotherapy. Confocal microscopy of the tumor tissue and resident lymphocytes in the presence of fluorescent tracers provides real-time monitoring of tumor response to various immunotherapy. The platform and accompanying analysis methods distinguish between a positive immune response and a lack of tissue response in the presence of immunotherapeutic agents.

This platform introduces novel methodologies in modeling and analyzing tumor response to improve prediction of patient-specific immunotherapy efficacy. To the best of our knowledge, this is the first report of human tumor fragments cultured in a dynamic perfusion system capable of testing the effect of circulating immune checkpoint inhibitors on resident tumor-infiltrating lymphocytes.

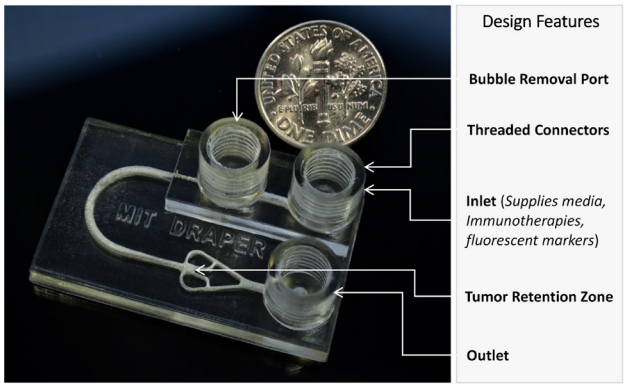

▲Figure 1: An optical picture of a 3D-printed, transparent, non-cytotoxic microfluidic platform for analysis of the efficacy of immunotherapy, with features labeled.

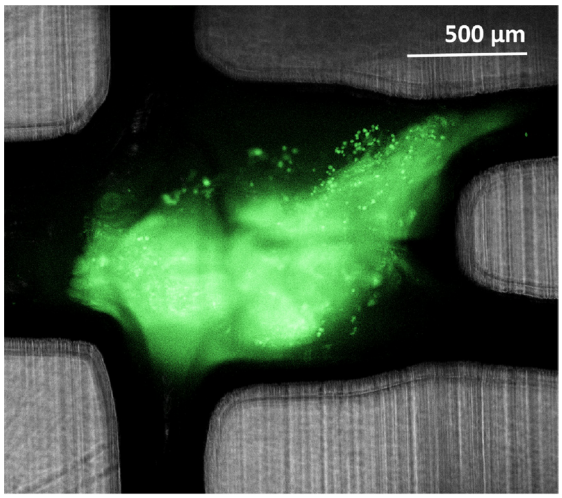

▲Figure 2: Overlaid bright-field and fluorescence images enable visualization of device geometries in addition to the stained tumor fragment. Single cells are visible.

FURTHER READING

- A. L. Beckwith, J. T. Borenstein, and L. F. Velásquez-García, "Monolithic, 3D-Printed Microfluidic Platform for Recapitulation of Dynamic Tumor Microenvironments," *Journal of Microelectromechanical Systems*, vol. 27, No. 6, pp. 1009-01022, Dec. 2018.
- A. L. Beckwith, L. F. Velásquez-García, and J. T. Borenstein, "Microfluidic Model for Evaluation of Immune Checkpoint Inhibitors in Human Tumors," *Advanced Healthcare Materials*, 2019.

Electrohydrodynamic Printing of Ceramic Piezoelectric Films for High-frequency Applications

B. García-Farrera, L. F. Velásquez-García
Sponsorship: MIT-Tecnológico de Monterrey Nanotechnology Program

The high operating frequencies that ceramic piezoelectric ultra-thin films attain have made possible exciting applications such as energy harvesting, telecommunications' filters, high sensitivity biosensors, and acoustofluidic devices; however, the inherently high cost and complexity of current manufacturing methods limit, in general, their widespread use. Additive manufacturing (AM), which has proven successful in creating complex devices and components of relevance to micro and nanosystems, could overcome these disadvantages; nevertheless, AM of piezoelectrics has been achieved only with polymer-based materials–unsuitable for said applications.

We report the first additively manufactured ceramic ultra-thin piezoelectric films compatible with high-frequency applications using electrohydrodynamic deposition (EHD) at room temperature. The films were made by electrospraying a zinc oxide (ZnO) nanoparticle liquid feedstock, directly writing line imprints as thin as 213 nm and as narrow as 198 µm.

We harness a previously unreported effect to align the polar axis of the imprint and obtain overall piezoelectricity. As Figure 1a shows, the (100) orientation monotonically increases as the linear density of the deposition is reduced by increasing the raster speed or reducing the feedstock flow rate (Q)–provided two conditions are met: the feedstock is ionized (via EHD), and a small separation between emitter and substrate is used. Notably, the orienting effect directly acts on the direction of the polar axis by means of the rastering direction (Figure 2a), allowing for vibration modes and resonator configurations that were previously unfeasible. The macroscopic piezoelectric behavior is shown through piezoforce response microscopy (PFM) (Figure 2b) and the suitability for high-frequency applications was demonstrated by testing thin-film bulk acoustic resonators (FBAR) on a flexible polymer substrate, where the resonant frequency of ~5 GHz was used to calculate the acoustic speed of the films (~2,000 m/s), which is close to the transversal wave speed of ZnO.

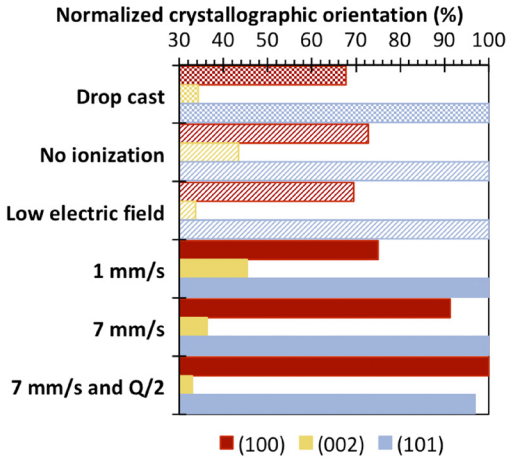

▲ Figure 1: Main crystallographic orientations for ZnO, normalized as a percentage of the highest peak. Fill patterns: reference (checkerboard), no impact on crystallography (dashes) and successful conditions (solid).

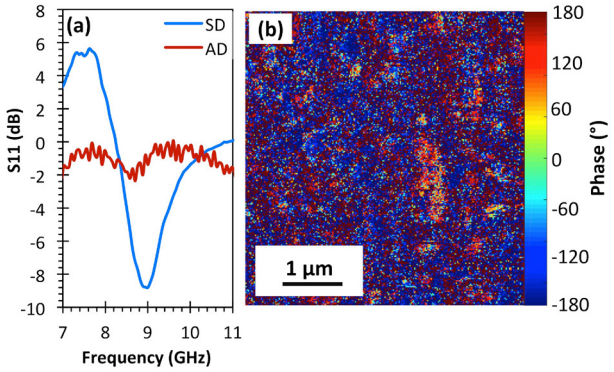

▲ Figure 2: (a) Frequency response of the reflection coefficient (S11) for laterally excited FBARs with films made of traces printed in the same (SD) or alternating (AD) directions. (b) 2D phase mapping of PFM. All films were printed at 3 mm/s.

FURTHER READING

- B. García-Farrera and L. F. Velásquez-García, "Room Temperature Direct Writing of Ultrathin Zinc Oxide Piezoelectric Films via Near-field Electrohydrodynamic Jetting for High-frequency Flexible Electronics," [to be presented] Transducers 2019–EUROSENSORS XXXIII, Germany, Jun. 2019.
- A. P. Taylor and L. F. Velásquez-García, "Electrospray-printed Nanostructured Graphene Oxide Gas Sensors," *Nanotechnology*, vol. 26, pp. 505301:1–8, Nov. 2015.
- A. P. Taylor, C. V. Cuervo, D. P. Arnold, and L. F. Velásquez-García, "Fully 3D-Printed, Monolithic Magnetic Actuators for Low-cost, Compact Systems," *J. of Microelectromechanical Systems*, doi:10.1109/JMEMS.2019.2910215, 2019.

3D-Printed, Monolithic, Multi-tip MEMS Corona Discharge Ionizers

Z. Sun and L. F. Velásquez-García
Sponsorship: MIT-Skoltech Next Generation Program

A corona discharge is a high-electric field ionization phenomenon caused by the development of a self-sustained electron avalanche between a sharp electrode (i.e., *corona* electrode) and a blunt electrode; the ions create a plasma region around the corona electrode and in their travel to the opposite electrode transfer momentum to the surrounding fluid. In this project, we are harnessing advanced metal inkjet printing technology to demonstrate massively multiplexed MEMS corona discharge ionizers (Figure 1), with the aim to increase greatly their ionization throughput and optimize their transduction mechanism to be able to implement exciting applications such as no-moving-parts pumps for gases and compact ion mobility spectrometers.

A 1D electrohydrodynamic coaxial cylinder model was implemented in COMSOL Multiphysics to study the ionization and collision processes in air at atmospheric pressure and room temperature of a 1-tip device, predicting a 400-µm-thick corona region surrounding the corona tip. The onset voltage estimated from the simulation is 5.849 kV, which is close to the theoretical value from Peek's formula of 6.416 kV. In addition, current over voltage (I/V) versus bias voltage minus the onset voltage (V-V_0) characteristics were collected for different ionizer array designs while varying the separation between the corona electrode and the collector electrode; the data follow the Townsend current-voltage model (Figure 2). Moreover, the data show that the corona current decreases with increased spacing of the corona electrode-to-collector electrode due to the decrease of the electric field on the tips; however, a smaller separation between the corona electrode and the collector electrode results in larger fluctuations in the corona discharge current. Devices with different numbers of tips tend to generate the same total corona current at the same bias voltage although more tips are set to discharge as the number of tips increases; this increase can be ascribed to the stronger interference between adjacent tips when the tip-to-tip spacing decreases. Current research efforts focus on optimizing the array design to minimize electric field shadowing and sharpening the tips to achieve operation at a lower bias voltage.

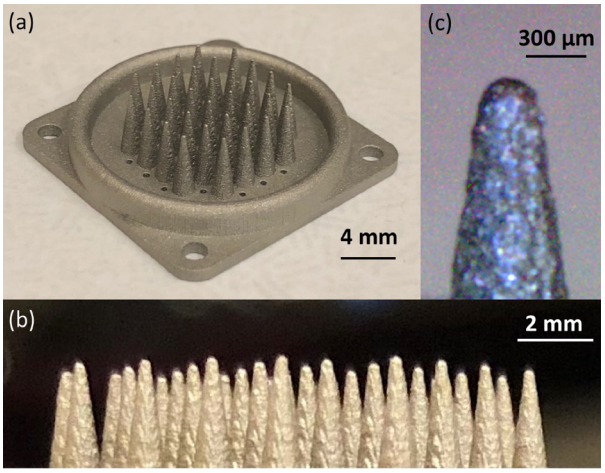

▲ Figure 1: Tilted view (a) and near-front view (b) of a binder inkjet-printed SS 316L planar array with 32 high-aspect-ratio tips; close-up top view of a tip (c).

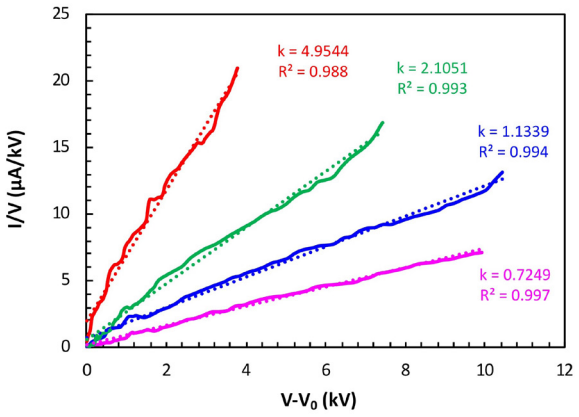

▲ Figure 2: I/V vs. (V-V_0) characteristics for a 5-emitter ionizer with 7.95-mm (red), 11.12-mm (green), 14.30-mm (blue), and 17.47-mm (magenta) electrode separation.

FURTHER READING

- P. Ferrer and M. P. Tchonang, "Miniaturization of Electrostatic Ion Engines by Ionization and Acceleration Coupling," *J. Phys. D. Appl. Phys.*, vol. 44, no. 33, pp. 33520, Aug. 2011.
- Z. Sun, G. Vladimirov, E. Nikolaev, and L. F. Velásquez-García, "Exploration of Metal 3-D Printing for the Microfabrication of Freeform, Finely Featured, Mesoscaled Structures," *J. of Microelectromechanical Systems*, vol. 27, no. 6, pp. 1171–1185, Dec. 2018.
- Z. Sun and L. F. Velásquez-García, "Miniature, 3D-Printed, Monolithic Arrays of Corona Ionizers," *Technical Digest of the 18th International Conference on Micro and Nanotechnology for Power Generation and Energy Conversion Applications (PowerMEMS 2018)*, pp. 37, 2018.

3D-Printed Gas Ionizer with CNT Cathode for Compact Mass Spectrometry

C. Yang, L. F. Velásquez-García
Sponsorship: IARPA

Mass spectrometers are powerful chemical analytical instruments used to quantitatively characterize the composition of unknown samples via ionization and mass-to-charge ratio species sorting. However, mainstream mass spectrometers are large, heavy, power hungry, and expensive, limiting their applicability in real-time and in-situ applications. Gas molecules can be ionized via electron impact ionization (EII), for which a source of electrons, i.e., a cathode, is required. Cold cathodes emit electrons into a vacuum via quantum tunneling due to high surface electric fields that lower and narrow the barrier that traps electrons within the material; typically, high-aspect-ratio, nano-sharp tips are used to produce such fields with moderate bias voltages. Compared to thermionic cathodes, field emission electron sources have faster response and less power consumption. Compared to other field emitters, carbon nanotubes (CNTs) are less affected by back-ion bombardment and chemical degradation. There are numerous reports of gas ionizers with CNT cathodes EIIs; however, these devices are microfabricated using cleanroom technology and/or use ion-generating structures machined with standard technologies, affecting their cost and size.

In this project, we are harnessing additive manufacturing (AM) to develop novel electron impact ionizers that circumvent these challenges. AM has unique advantages over traditional manufacturing methods including compatibility with creating complex 3D geometries, print customization, and waste reduction. Our design (Figure 1) uses inkjet binder printing of SS 316L to create electrodes to efficiently generate ions and steer charged species, stereolithography of polymer resin to define the dielectric structures that electrically isolate the different electrodes, and an additively manufactured CNT electron source. We have successfully characterized the ionizers at pressures as high as 5 mTorr while achieving ionization efficiencies as high as 8.5% (Figure 2).

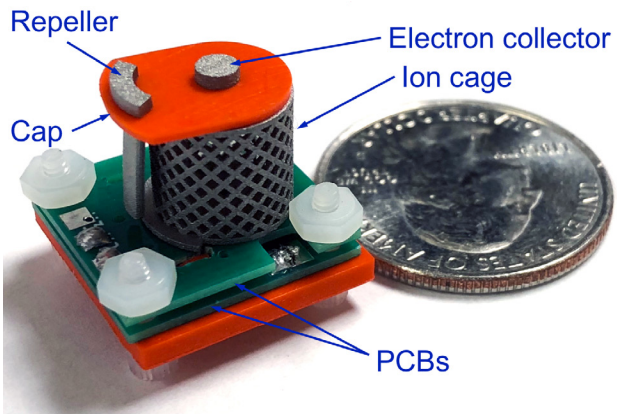

▲Figure 1: Fully additively manufactured electron impact gas ionizer with CNT cathode. Ion cage sets a region with uniform ionization cross section. Electron collector gathers electrons emitted by cathode and released during ionization. Ion repeller pushes ions out of ion cage. The cap interfaces with electrodes to create a 3D structure while providing electrical insulation.

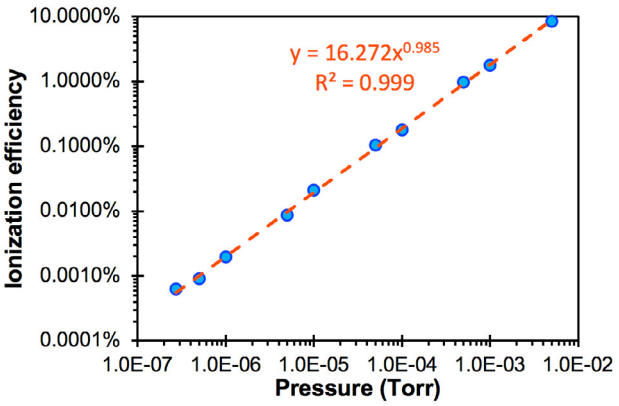

▲Figure 2: Ion current-to-transmitted electron current ratio versus pressure when field emission electron source of EII is biased at 700. There is linear dependence between pressure and ionization efficiency, in agreement with EII model.

FURTHER READING

- C. Yang and L. F. Velásquez-García, "Low-cost, Additively Manufactured Electron Impact Gas Ionizer with CNT Field Emission Cathode for Compact Mass Spectrometry," *J. of Physics D – Applied Physics*, vol. 52, no. 7, 075301, p. 9, Feb. 2019.
- L. F. Velásquez-García, B. Gassend, and A. I. Akinwande, "CNT-based MEMS Ionizers for Portable Mass Spectrometry Applications," *J. of Microelectromechanical Systems*, vol. 19, no. 3, pp. 484-493, Jun. 2010.
- B. Gassend, L. F. Velásquez-García, and A. I. Akinwande, "Precision In-plane Hand Assembly of Bulk-microfabricated Components for High-voltage MEMS Arrays Applications," *J. of Microelectromechanical Systems*, vol. 18, no. 2, pp. 332–346, Apr. 2009.

Printed CNT Field Emission Sources with Integrated Extractor Electrode

I. A. Perales-Martínez, L. F. Velásquez-García
Sponsorship: MIT-Tecnólogico

Field emission cathodes are promising electron sources for exciting applications such as flat-panel displays, free-electron lasers, and portable mass spectrometry where fast switching, low-pressure operation, and low power consumption are favored metrics. A field emitter quantum tunnels electrons to a vacuum due to the high electrostatic fields at its surface; this tunneling is typically done at low voltage using a whisker-like structure. Carbon nanotubes (CNTs) are attractive structures to produce electron field emission due to their ultrasharp tip diameter, high aspect ratio, high electrical conductivity, and excellent mechanical and chemical stability. Although CNT-based cold cathodes have been widely reported in the literature, their manufacture could be quite expensive (e.g., devices partially or fully made in a semiconductor cleanroom), or the extractor electrode of the cathode is an external mesh, causing high-beam interception (e.g., in screen-printed devices) or requiring an advanced method of assembly to the emitting component to achieve high transmission.

In this project, we are developing novel field emission sources that are fully additively manufactured to circumvent the aforementioned challenges. The devices are made via direct ink write (DIW) printing, which is one of the least expensive and most versatile additive manufacturing methods as is capable of monolithic multi-material printing. Compared to screen printing, DIW does not involve static masks to transfer patterns and produces significantly less waste. The fully-printed field emission electron source is composed of two continuous imprints: a spiral trace made of a CNT compound, acting as an emitting electrode, symmetrically surrounded on both sides by a spiral trace made of silver nanoparticles, acting as in-plane extractor electrode (Figure 1). After printing, the CNT spiral receives a mechanical treatment that releases the CNT tips from the bulk of the imprint (Figure 2), enabling field emission from the CNT imprint. Characterization of the printed CNT field emission sources in triode configuration (i.e., using an external anode) shows low turn-on voltage and low interception of the emitted current by the extractor electrode. Current work focuses on design optimization and experimental characterization of the devices.

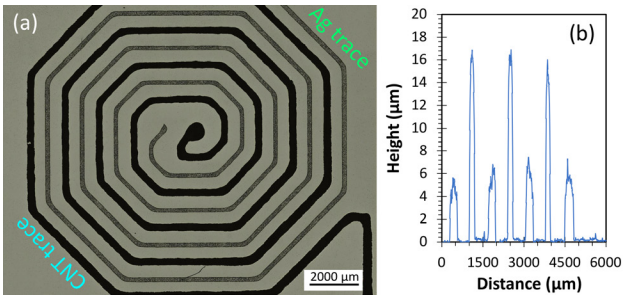

▲ Figure 1: Fully-printed CNT field emission source (a) and linear scan of structure in radial direction using confocal microscope (b). CNT traces are about 300 µm wide and 5 µm tall; Ag traces are about 200 µm wide and 16 µm tall.

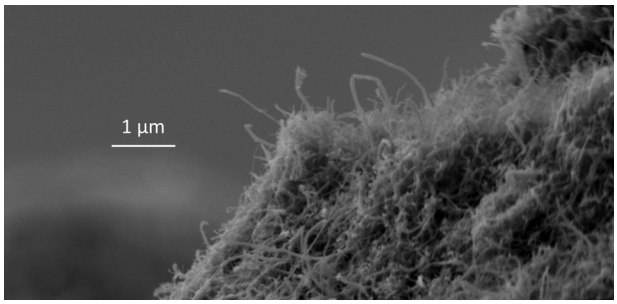

▲ Figure 2: Close-up scanning electron micrography of surface of CNT trace after mechanical treatment that releases CNTs from bulk is executed. Procedure creates grass-like structure suitable for field emission.

FURTHER READING

- C. Yang and L. F. Velásquez-García, "Low-cost, Additively Manufactured Electron Impact Gas Ionizer with CNT Field Emission Cathode for Compact Mass Spectrometry," *J. of Physics D – Applied Physics*, vol. 52, no. 7, 075301, p. 9, Feb. 2019.
- L. F. Velásquez-García, B. Gassend, and A. I. Akinwande, "CNT-based MEMS Ionizers for Portable Mass Spectrometry Applications," *J. of Microelectromechanical Systems*, vol. 19, no. 3, pp. 484-493, Jun. 2010.
- B. Gassend, L. F. Velásquez-García, and A. I. Akinwande, "Precision in-Plane Hand Assembly of Bulk-microfabricated Components for High voltage MEMS Arrays Applications," *J. of Microelectromechanical Systems*, vol. 18, no. 2, pp. 332–346, Apr. 2009.

Controlling the Nanostructure in Room-temperature-microsputtered Metal

Y. Kornbluth, R. Matthews, L. Parameswaran, L. M. Racz, L. F. Velásquez-García
Sponsorship: MIT Lincoln Laboratory

Sputter deposition involves the ejection of atoms from a target and the atoms' subsequent deposition on a nearby substrate. Because the deposition is done on the atomic level, the nanostructure of the deposit can vary significantly. This variance is of concern, as it can greatly affect material strength and conductivity. Traditional sputtering relies on vacuum and thermal annealing to ensure dense, highly conductive deposits. However, agile manufacturing on temperature-sensitive substrates is not compatible with these two solutions.

To enable high-quality material without heating the material or requiring a vacuum, we performed a statistically-motivated set of experiments to determine what deposition parameters improve the material quality. We developed an empirical model and found that an appropriate electrical bias voltage, applied either to the substrate or to a conductive plate under the substrate, has the greatest impact on the material quality. This is due to the presence of charged nanoparticles, formed by collisions between sputtered atoms in the dense plasma around the sputter target. The applied electric field attracts positively charged nanoparticles, allowing the nanoparticles to strike the substrate with more energy than their temperature alone would dictate. This extra energy enhances the mobility of the deposited metal, allowing it to form denser, more energetically favorable coatings (Figure 1) without significant substrate heating. With this technique, we have improved the conductivity of the sputter coating to 5x bulk metal (15 μΩ·cm) at room temperature.

Applied electric fields also improve the coating's thickness. In the absence of electric fields, the sputtering process is self-limiting. As the positively charged sputtered material reaches the substrate, charge builds upon the substrate, repelling charged sputtered material and preventing the deposit from thickening. However, biasing the substrate with a negative voltage prevents this charge from accumulating, allowing for thicker (> 200 nm) films.

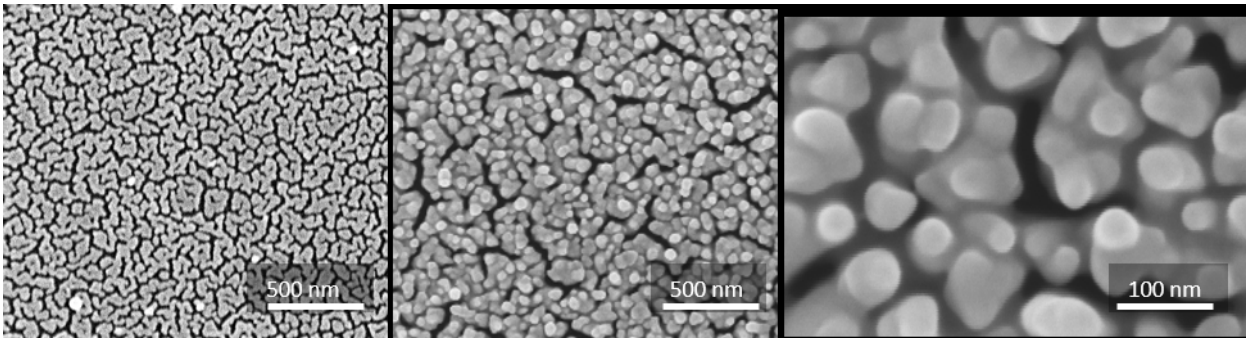

▲Figure 1: Deposit nanostructure without (left) and with (center, right) applied bias voltage (-500 V). The electric field attracts nanoparticles, allowing them to strike the substrate with sufficient energy to rearrange into an energetically favorable, dense nanostructure, resulting in high electrical conductivity of the imprint.The voids in the right-hand side image are due to the limited depth of focus of the electron microscope.

FURTHER READING

- Y. Kornbluth, R. H. Mathews, L. Parameswaran, L. Racz, and L. F. Velásquez-García, "Room-temperature, Atmospheric-pressure Deposition of Dense, Nanostructured Metal Films via Microsputtering," *Nanotechnology*, vol. 30, No. 28, 285602 (10pp), Jul. 2019.
- Y. Kornbluth, R. H. Mathews, L. Parameswaran, L. M. Racz, and L. F. Velásquez-García, "Microsputterer with Integrated Ion-drag Focusing for Additive Manufacturing of Thin, Narrow Conductive Lines," *J. of Physics D – Applied Physics*, vol. 51, no. 16, p. 165603, Apr. 2018.
- R. Messier, A. P. Giri, and R. A. Roy, "Revised Structure Zone Model for Thin Film Physical Structure," *JVST A*, vol. 2, p. 500, 1984.

Gated Silicon Field Ionization Arrays for Compact Neutron Sources

G. Rughoobur, A. I. Akinwande
Sponsorship: Defense Advanced Research Projects Agency

Neutron radiation is widely used in various applications, ranging from the analysis of the composition and structure of materials and cancer therapy to neutron imaging for security. However, most applications require a large neutron flux that is often achieved only in large infrastructures such as nuclear reactors and accelerators. Neutrons are generated by ionizing deuterium (D_2) to produce deuterium ions (D^+) that can be accelerated towards a target loaded with either D or tritium (T). The reaction generates neutrons and isotopes of He, with the D-T reaction producing the higher neutron yield. Classic ion sources require extremely high positive electric fields, on the order of 10^8 volts per centimeter (10 V/nm). Such a field is achievable only in the vicinity of sharp electrodes under a large bias, and consequently, ion sources for neutron generation are bulky.

This work explores, as an alternative, highly scalable and compact Si field ionization arrays (FIAs) with a unique device architecture that uses self-aligned gates and a high-aspect-ratio (~40:1) silicon nanowire current limiter to regulate electron flow to each field emitter tip in the array (Figure 1). The tip radius has a log-normal distribution with a mean of 5 nm and a standard deviation of 1.5 nm, while the gate aperture is ~350 nm in diameter and is within 200 nm of the tip. Field factors, β, > 1 × 10^6 cm^{-1} can be achieved with these Si FIAs, implying that gate-emitter voltages of 250-300 V (if not less) can produce D^+ based on the tip field of 25-30 V/nm. In this work, our devices achieve ionization current of up to 5 nA at ~140 V for D_2 at pressures of 10 mTorr. Gases such as He and Ar can also be ionized at voltages (<100 V) with these compact Si FIAs (Figure 2).

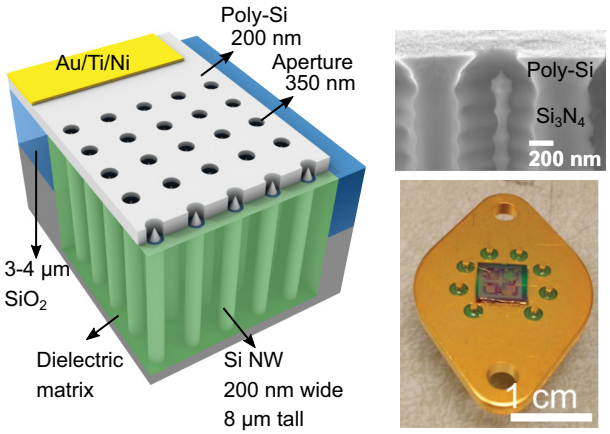

▲ Figure 1: Schematic of gated field ionization array, with SEM cross-section of a single field ionizer and photograph of a packaged chip with arrays of different sizes for neutron generation

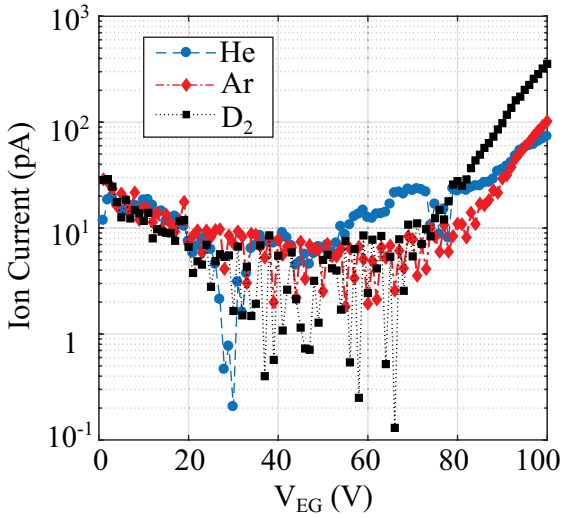

▲ Figure 2: Ion current measured for different gases (He, Ar, and D_2) at 1 mTorr pressure demonstrating low ionization voltages using 1000 by 1000 Si FIAs.

FURTHER READING

- M. Araghchini, S. A. Guerrera, and A. I. Akinwande, "High Current Density MEMS Deuterium Ionizers," *2016 29th International Vacuum Nanoelectronics Conference*, pp. 1–2, 2016.
- A. Fomani, L. F. Velasquez-Garcia, and A. I. Akinwande, "Low-voltage Field Ionization of Gases up to Torr-level Pressures using Massive Arrays of Self-aligned Gated Nanoscale Tips," *IEEE Trans. Electron Devices*, vol. 61, no. 5, pp. 1520–1528, 2014.
- Bargsten Johnson, P. R. Schwoebel, P. J. Resnick, C. E. Holland, K. L. Hertz, and D. L. Chichester, "Field Ionization Characteristics of an Ion Source Array for Neutron Generators," *J. Appl. Phys.*, vol. 114, no. 17, p. 174906, Nov. 2013.

Silicon Field Emitter Arrays (FEAs) with Focusing Gate and Integrated Nanowire Current Limiter

G. Rughoobur, L. Jain, A. I. Akinwande
Sponsorship: Air Force Research Laboratory, Intelligence Advanced Research Projects Activity

The advent of microfabrication has enabled scalable and high-density Si field emitter arrays (FEAs). These are advantageous due to compatibility with complementary metal-oxide-semiconductor (CMOS) processes, the maturity of the technology, and the ease in fabricating sharp tips using oxidation. The use of a current limiter is necessary to avoid burn-out of the sharper tips. Active methods using integrated MOS field-effect transistors and passive methods using a nano-pillar (~200 nm wide, 8 µm tall) in conjunction with the tip have been demonstrated. Si FEAs with single gates reported in our previous works have current densities >100 A/cm² and operate with lifetimes of over 100 hours.

The need for another gate (Figure 1) becomes essential to control the focal spot size of the electron beam as electrons leaving the tip have an emission angle of ≈ 12.5°. The focus electrode provides a radial electric field that reduces the lateral velocity of stray electrons and narrows the cone angle of the beam reaching the anode. Varying the voltage on the focus gate reduces the focal spot size or achieves an electron beam modulator for radio frequency applications. In this work, we fabricate dense (1-µm pitch) double-gated Si with an integrated nanowire current limiter (Figure 2). The apertures are ~350 nm and ~550 nm for the extractor and focus gates, respectively, with a 350-nm-thick oxide insulator separating the two gates. Electrical characterization of the fabricated devices shows that the focus-to-gate ratio (V_{FE}/V_{GE}) can be used to control the anode current (Figure 2). When the focus voltage exceeds the gate voltage, the field superposition increases the extracted current, and vice versa. These devices can potentially find applications as high-current focused electron sources in flat panel displays, nano-focused X-ray generation, and microwave tubes.

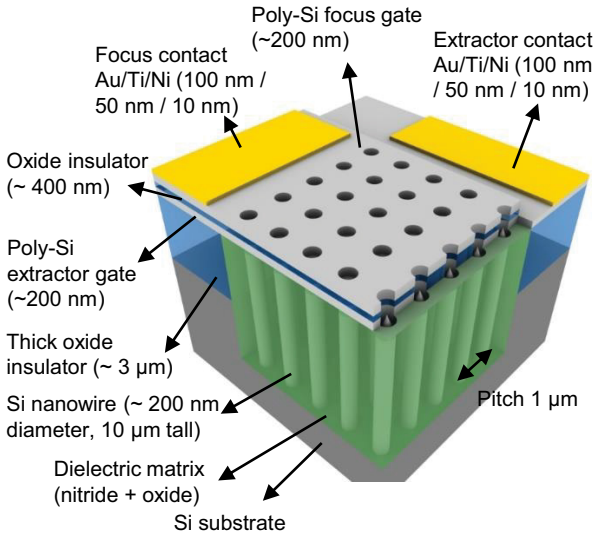

▲ Figure 1: Si field emitter array with integrated current limiter, self-aligned extractor, and focus gates for nano-focused cold electron sources.

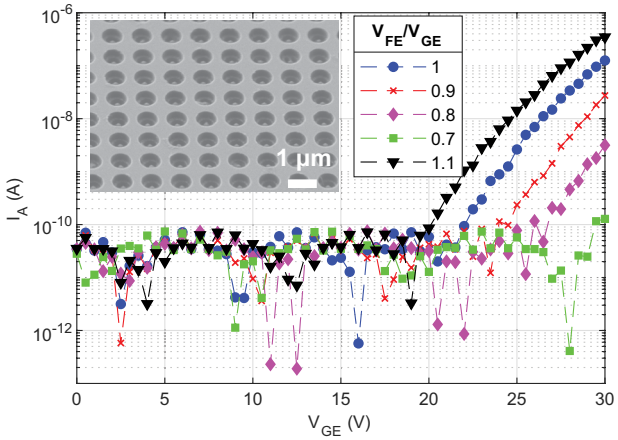

▲ Figure 2: Electrical characterization of 500 by 500 arrays with different focus/gate voltage ratios at 1000 V anode, inset shows the fabricated double-gated array.

FURTHER READING

- S. A. Guerrera and A. I. Akinwande, "Nanofabrication of Arrays of Silicon Field Emitters with Vertical Silicon Nanowire Current Limiters and Self-aligned Gates," *Nanotechnology*, vol. 27, no. 29, p. 295302, Jul. 2016.
- L. Y. Chen and A. I. Akinwande, "Aperture-collimated Double-gated Silicon Field Emitter Arrays," *IEEE Trans. Electron Devices*, vol. 54, no. 3, pp. 601–608, 2007.
- L. Dvorson, I. Kymissis, and A. I. Akinwande, "Double-gated Silicon Field Emitters," *J. Vac. Sci. Technol. B Microelectron. Nanom. Struct.*, vol. 21, no. 1, p. 486, 2003.

Highly Uniform Silicon Field Emitter Arrays

N. Karaulac, A. I. Akinwande
Sponsorship: Defense Advanced Research Projects Agency, Intelligence Advanced Research Projects Activity

Cold cathodes based on silicon field emitter arrays (FEAs) have shown promise in a variety of applications requiring high-current-density electron sources. However, FEAs face a number of challenges that have prevented them from achieving widespread use in commercial and military applications. One problem limiting the reliability of FEAs is emitter tip burnout due to Joule heating. The current fabrication process for FEAs results in a non-uniform distribution of emitter tip radii. At a fixed voltage, emitters with a small radius emit a higher current while emitters with a large radius emit a lower current. Therefore, emitters with a small radius reach their thermal limit due to Joule heating at lower voltages and consequently burn out. Previous solutions to tip burnout have focused on limiting the emitter current with resistors, transistors, or nanowires to obtain more uniform emission current.

In this project, we focused on increasing the uniformity of emitter tip radii as a means to reduce tip burnout. Figure 1 shows a typical distribution of emitter tip radii for FEAs. The non-uniform distribution of emitter tip radii first forms during the photolithography step that defines the array of "dots" that become the etching mask for the silicon tips. In our FEA fabrication process, we used a trilevel resist process that nearly eliminated the light wave reflected at the photoresist/silicon interface and hence improved the uniformity of the dot diameter. Furthermore, we integrated the emitter tips with silicon nanowires to improve their reliability. Figure 2 shows a diagram of the fabricated structure. Our fabrication process resulted in FEAs with more uniform emission current and potentially a longer lifetime.

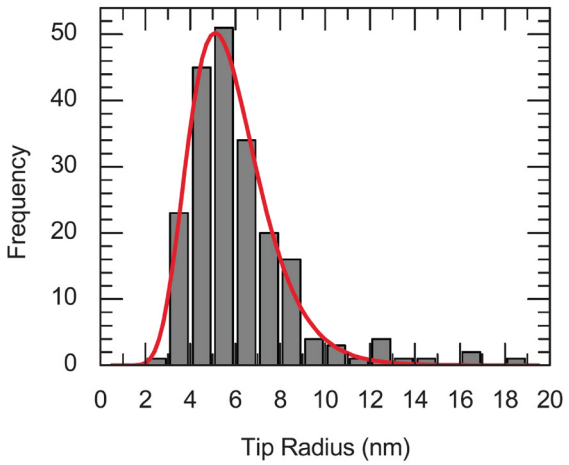

▲Figure 1: Non-uniform distribution of emitter tip radii resulting from the fabrication process of silicon FEAs.

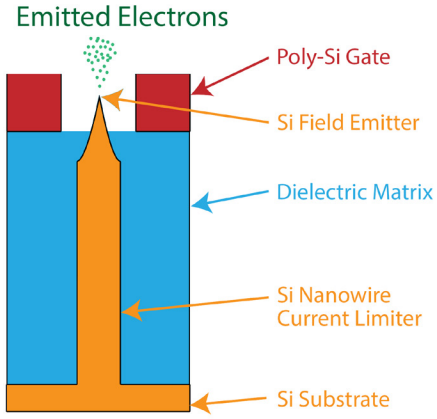

▲Figure 2: Cross-sectional diagram of a silicon field emitter. The emitter tip sits on top of a high-aspect-ratio silicon nanowire that limits the field emission current from the tip.

FURTHER READING

- S. A. Guerrera and A. I. Akinwande, "Nanofabrication of Arrays of Silicon Field Emitters with Vertical Silicon Nanowire Current Limiters and Self-aligned Gates," *Nanotechnology*, vol. 27, no. 29, pp. 295302:1-11, Jul. 2016.
- M. L. Schattenburg, R. J. Aucoin, and R. C. Fleming, "Optically Matched Trilevel Resist Process for Nanostructure Fabrication," *J. of Vacuum Science & Technology B: Microelectronics and Nanometer Structures*, vol. 13, no. 6, p. 3007, Nov. 1995.

Development of a Subnanometer-Precision Scanning Anode Field Emission Microscope

O. O. Ilori, A. I. Akinwande
Sponsorship: Air Force Office of Scientific Research

Field emitter arrays (FEA) have not found widespread adoption in demanding applications such as THz, RF, Deep UV, X-ray, electron, ion, and neutron sources, where high current (>1 mA) and long operating lifetime (>10,000 hrs.) are required. These limitations arise as a result of the sensitivity of emitted electron and ion current to the spatial non-uniformity of emitter tip radius and the temporal non-uniformity of work function due to adsorption and desorption of gas molecules at the surface of the emitter tips. These non-uniformities result in the variation of the field factor (β), a key performance parameter for field emitters and ionizers. Variations in β result in severe underutilization of emitter tips as only few tips with large β contributes to emission or ionization current. These tips, if not protected, burn out, leading to low emission current and very short operation lifetime. Emission current and operational lifetime of a FEA could thus be improved by making emitters with more uniform characteristics.

We are developing a subnanometer-precision scanning anode field-emission microscope (SAFEM) that could be used to probe the fundamental processes in the operation of emitter tips of FEA. The SAFEM is designed to precisely and accurately position, with subnanometer resolution, a probing anode over the tips of an FEA and in scanning mode directly acquire the spatial map of emission tip current. From the map, other characteristics of the emitter tip such as anode voltage, tip radius, density, and field factor can be extracted. The map of extracted parameters could yield insight into the operation of the FEAs. Also, a statistical distribution of the field factor will enable study of the dependence of tip characteristics on the fabrication process and thereby enable exploration of novel process for engineering high-performance FEAs with high current densities and long operational lifetimes.

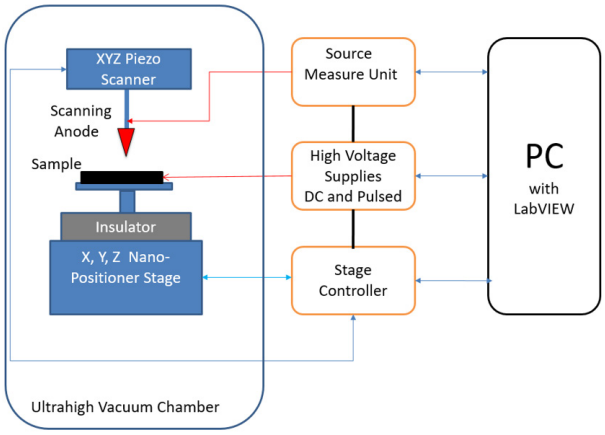

▲ Figure 1: Schematic of the SAFEM.

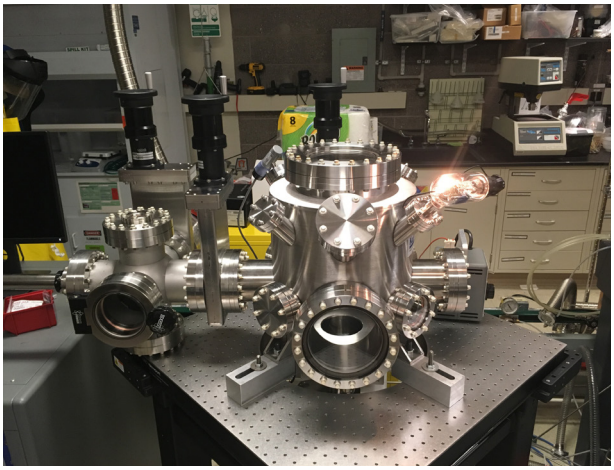

▲ Figure 2: The SAFEM UHV chamber and subnano positioner stage.

FURTHER READING

- L. Nilsson, O. Groening, P. Groening, O. Kuettel, and L. Schlapbach, "Characterization of Thin Film Electron Emitters by Scanning Anode Field Emission Microscopy," *J. of Applied Physics*, vol. 90, no. 2, pp. 768–780, Jul. 2001.
- T. Wang, C. E. Reece, and R. M. Sundelin, "Direct Current Scanning Field Emission Microscope Integrated with Existing Scanning Electron Microscope," *Review of Scientific Instruments*, vol. 73, no. 9, pp. 3215–3220, Sep. 2002.
- F. Andrianiazy, J.-P. Mazellier, L. Sabaut, L. Gangloff, P. Legagneux, and O. Gröning, "Quantitative Characterization of Field Emission Parameters: Application to Statistical Analysis of Individual Carbon Nanotubes/Nanofibers," *J. of Vacuum Science & Technology B*, vol. 33, no. 1, p. 012201, Nov. 2014.

Nanoscale Vacuum Channel Transistors Operation in Poor Vacuum

G. Rughoobur, L. Jain, A. I. Akinwande
Sponsorship: Air Force Office of Scientific Research, Multidisciplinary University Research Initiatives

Nanoscale vacuum channel transistors (NVCTs) using field emission sources could potentially have superior performance compared to solid-state devices of similar channel length. This superior performance is due to ballistic transport of electrons, shorter transit time, and higher breakdown voltage in vacuum. Furthermore, there is no opportunity for ionization or avalanche carrier multiplication imbuing NVCTs with very high Johnson figure of merit (~10^{14} V/s). However, field emitters need ultra-high vacuum (UHV) for reliable operation as the field emission process is sensitive to barrier height variations induced by adsorption/desorption of gas molecules. Small changes in the barrier height cause exponential variations in current. Poor vacuum also leads to the generation of energetic ions that bombard the emitters, altering their work function and degrading electrical performance.

Graphene can be used to nano-encapsulate the field emitter in UHV or a gas (e.g., He) with high ionization energy to overcome the UHV requirement. Separation of the electron tunneling region from the electron acceleration region enables emission of electrons in UHV and electron transport in poor vacuum, if not atmospheric conditions. For mechanical strength, a multi-layer graphene structure that is transparent to electrons while being impervious to gas molecules/ions is necessary.

In this work, we studied the electron transparency and robustness of multi-layer graphene. We fabricated arrays of gated Si field emitters with 1-µm pitch and integrated a nanowire current limiter (Figure 1) that exhibits transistor-like characteristics. Using an energized multi-layer graphene/grid structure (Figure 2) in combination with emitter arrays, we achieved an electron transparency of ≈ 20%. We envision electron transparencies close to ~100% with an optimized design. Adopting this architecture for NVCTs will allow the realization of empty state electronics capable of functioning at higher frequencies (THz regime), higher power, and harsher conditions (high radiation and high temperature) than solid-state electronics.

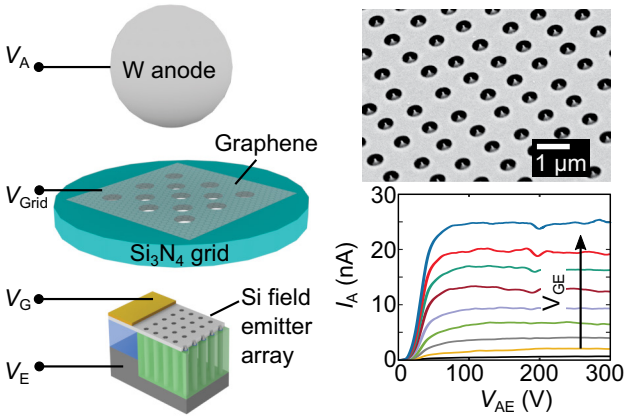

▲Figure 1: Schematic of the measurement set-up with the graphene on the nitride grid, SEM image of arrays of gated nanotips and transistor behavior of field emitter array from V_{GE} = 22 V to 30 V.

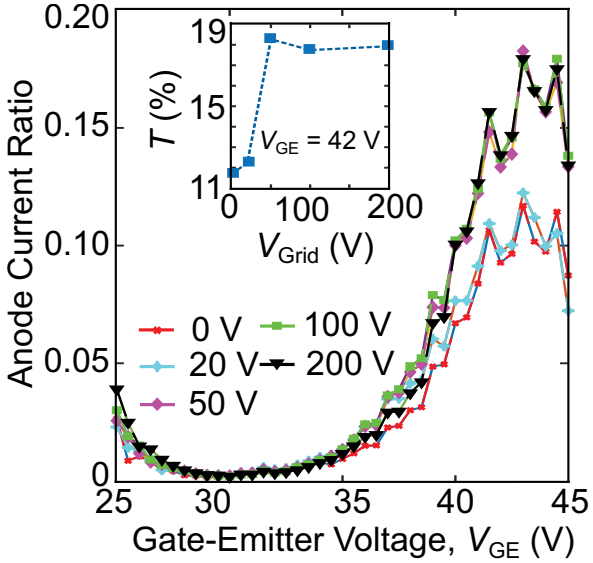

▲Figure 2: Anode current ratio (100 by 100 array) with multi-layer of graphene to no grid/graphene case, with inset showing the percentage transmission through the structure.

FURTHER READING

- S. A. Guerrera and A. I. Akinwande, "He Channel NanoTransistors — Towards 'Vacuum-less' Empty State Electronics," *2016 29th International Vacuum Nanoelectronics Conference*, pp. 1–2, 2016.
- S. Bunch, S. S. Verbridge, J. S. Alden, A. M. Van Der Zande, J. M. Parpia, H. G. Craighead, and P. L. Mceuen, "Impermeable Atomic Membranes from 2008," *Nano Lett.*, vol. 8, p. 2458–2462, 2008.
- J.-W. Han, D.-I. Moon, and M. Meyyappan, "Nanoscale Vacuum Channel Transistor," *Nano Lett.*, vol. 17, no. 4, pp. 2146–2151, Apr. 2017.

Micro Rocket Engine using Steam Injector and Peroxide Decomposition

J. Protz
Sponsorship: Protz Lab Group; microEngine, LLC; Asteria Propulsion, LLC

Rocket engines miniaturized and fabricated using silicon MEMS have been an active area of research for two decades. At these scales, miniaturized steam injectors like those used in Victorian-era steam locomotives are viable as a pumping mechanism and offer an alternative to pressure feed and high-speed turbo-pumps. Storing propellants at low pressure reduces tank mass, and this improves the vehicle empty-to-gross mass ratio; if one propellant is responsible for most of the propellant mass (e.g., oxidizer), injecting it while leaving the others solid or pressure-fed can still achieve much of the potential gain. Previously, the PI and his group demonstrated the feasibility of this pumping concept by designing and testing two ultraminiature-machined stainless steel micro jet injectors that pumped ethanol and by exploring liquid bi-propellant engine designs.

Current efforts focus on designing a test article and fabrication process that integrates a jet injector, a decomposition chamber, and a thrust chamber with a solid or liquid fuel to form an injector-pumped partially-pressure-fed or hybrid micro rocket (see Figures 1 and 2). The proposed demonstration launch vehicle integrates these with suitably-sized propellant tanks and structures, derived from or like those found in hobby rocketry. Other applications have also been explored.

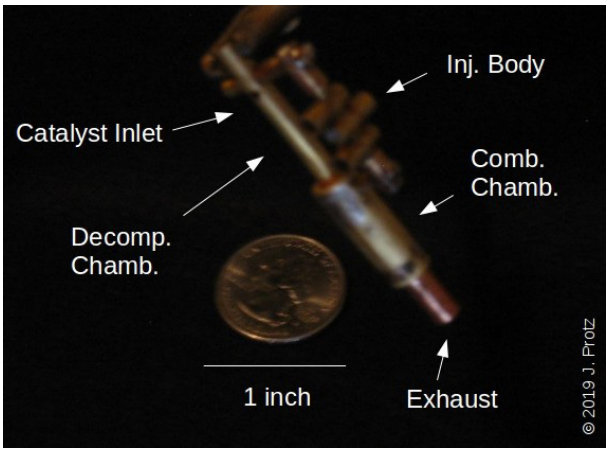

▲ Figure 1: Brass-engineering mock-up of integrated engine, with decomposition chamber, thrust chamber, and injector body.

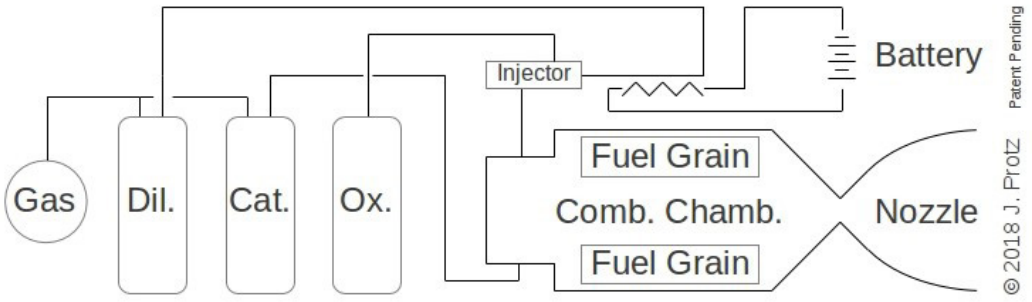

▲ Figure 2: Schematic diagram of an injector-pumped micro rocket with tanks and engine.

FURTHER READING

- J. M. Protz, "Progress towards an Injector-Pumped Micro Rocket Engine and Vehicle," invited talk to Gas Turbine Laboratory, MIT, Cambridge, MA, May 7, 2019.
- J.M. Protz, "Giffard-Injector-Pumped Microrockets," invited talk to Dept. of Mech. Eng., MIT, Cambridge, MA, USA, May 2010.
- J. M. Protz, "Modeling and Analysis of a Giffard-Injector-Pumped Bipropellant Microrocket," invited talk to Pratt & Whitney Rocketdyne, Huntsville, AL, February 3, 2010.

Ptychography Development for Soft X-ray Imaging at the Nanoscale

A. Levitan, J. Li, R. Comin

Ptychography, a powerful imaging modality, has been applied successfully to many experimental systems. Ptychography visualizes an extended object via retrieval of the far-field phases of a wave scattered from it, from which a complex Fourier transform is extracted and a real space image formed by simple Fourier inversion. Removing the need for a high-quality imaging optic, ptychography improves the resolution of microscopy experiments using high-energy probes, e.g., x-ray and electron microscopy, where lens quality limits accuracy. Ptychography also enables quantitative phase contrast imaging. X-ray ptychography in the Bragg geometry enables high-spatial-resolution quantitative studies of nanoscale structures in most electronic and magnetic materials: bulk crystals, thin films, heterointerfaces, or composite devices. However, inevitable contamination by experimental sources of error limits progress in this area.

X-ray ptychography requires high source coherence, monochromaticity, and stability plus precision motion of the source-forming optics. Studying electronic phases with soft x-rays in the Bragg geometry requires high vacuum, a stable cryogenic sample environment, and a full diffractometer; experiments inevitably face multiple serious sources of error. This challenge has deterred serious effort in this direction, despite enormous scientific potential. Intimate knowledge of these issues enabled us to develop computational tools to handle multiple qualitatively different sources of error simultaneously. We define experiment-specific forward models that incorporate parameters describing the dominant sources of error. Applying automatic differentiation and gradient descent-based optimization algorithms such as *Adam* allows reconstruction of contributions to the error during reconstruction of sample features.

We validated our automatic differentiation-based approach with a series of proof-of-concept experiments at the CSX beamline of the National Synchrotron Light Source II (Brookhaven Natl Lab) in transmission and Bragg geometries. Experimental issues included extreme probe positioning errors, large fluctuations in the probe fluence, and reduced probe coherence. We successfully reconstructed test samples with known structures and produced consistent high-quality reconstructions from more realistic samples (see Figure 1). Future directions include studies of electronic symmetry breaking that are enabled by this novel capability, improvements to various error sources, and the ultimate resolution of the reconstructed images.

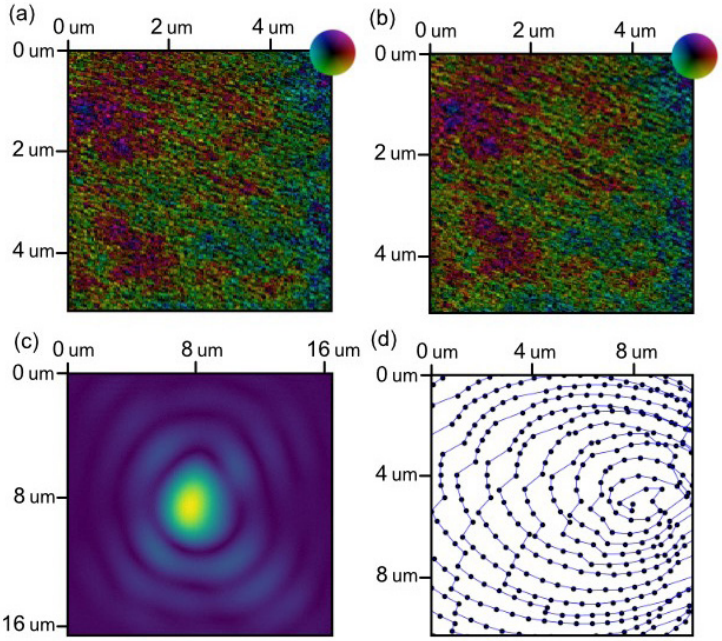

▲ Figure 1: (a) and (b) Complex magnetic domain images of the same spot on a sample of NdNiO3, reconstructed from completely independent datasets. Both datasets were collected in the Bragg geometry. The amplitude is associated with the domain map, hue to phase contrast. (c) Amplitude of the associated probe reconstruction. (d) Associated probe position reconstruction, demonstrating the extent (roughly 500 nm) of positional errors.